Remote Sensing of Environment 169 (2015) 290–306

Contents lists available at ScienceDirect

Remote Sensing of Environment

journal homepage: www.elsevier.com/locate/rse

Mapping ground deformation over Houston–Galveston, Texas using multi-temporal InSAR

Feifei Qu [a,b], Zhong Lu [b,*], Qin Zhang [a], Gerald W. Bawden [c], Jin-Woo Kim [b], Chaoying Zhao [a], Wei Qu [a]

[a] College of Geology Engineering and Geomatics, Chang'an University, No. 126 Yanta Road, Xi'an 710054, China
[b] Huffington Department of Earth Sciences, Southern Methodist University, Dallas, TX 75275, USA
[c] U.S. Geological Survey, 3020 State University Dr. East, Sacramento, CA 95819, USA

ARTICLE INFO

Article history:
Received 10 March 2015
Received in revised form 16 August 2015
Accepted 23 August 2015
Available online xxxx

Keywords:
InSAR
Multi-temporal InSAR
Subsidence
Aquifer
Fault
Oil field
Salt dome
Houston

ABSTRACT

Houston–Galveston (HG) region in Texas has been subsiding due to the combined effects of groundwater withdrawal, hydrocarbon extraction, salt dome movement, and faulting. This human- and partially nature-induced ground deformation has gradually threatened the stability of urban infrastructure and caused the loss of wetland habitat along the Gulf of Mexico. Interferometric synthetic aperture radar (InSAR) techniques can measure ground motions in high spatial resolution over large coverage. The purpose of this study is to map the spatial and temporal variations in surface deformation around the HG region using a Multi-Temporal InSAR (MTI) technique and to assess the role of fluid withdrawal (groundwater withdrawal and hydrocarbon extraction), salt tectonics, and fault activity in land surface deformation. MTI-derived land surface deformation measurements are then compared to GPS and extensometer observations, geologic and hydrologic data, and information about hydrocarbon extraction to address the causes of the observed deformation. The MTI measurements based on ERS-1/2 datasets have mapped regional subsidence up to 53 mm/yr in the northwestern HG as well as a slight uplift at 20 mm/yr in the southeastern HG from 1993 to 2000. InSAR measurements obtained from Envisat and ALOS data reveal subsidence rate of up to 30 mm/yr over the northwestern HG between 2004 and 2011. Our results indicate that the pattern of ground deformation was nearly concentric around locations of intense groundwater withdrawal and the spatial extent of the subsiding area has been shrinking and migrating toward the northeast after 2000. We have resolved localized ground subsidence cones over hydrocarbon exploration fields, which were likely caused by reservoir compaction. We have differentiated ground surface deformation over salt domes, which was due to ongoing differential movement of individual salt spines. We have identified 5–40 mm/yr differential subsidence across a number of faults in the region. These faults functioned as water barriers disrupting the integrity of ground water flow and aggravating localized surface displacements.

1. Introduction

The Houston–Galveston (HG) region, comprising Harris, Galveston, Fort Bend, Montgomery, Brazoria, Liberty, San Jacinto, Walker, Grimes, Waller, and Chambers Counties (Fig. 1), has been negatively affected by surface deformation -especially subsidence- for decades. By 1979, as much as 3 m of subsidence had occurred in the HG region and approximately 8300 km^2 of land subsided more than 0.3 m (Coplin & Galloway, 1999). Over the southeastern Harris County, the maximum subsidence reached 4 m during the 1915–17 and 2001 period. Land-surface subsidence caused by fluid withdrawals was firstly documented in the HG area in conjunction with the Goose Creek oil field in southeastern Harris County (Pratt & Johnson, 1926). Subsidence continued throughout the 20th century as a result of groundwater withdrawal that depressed the major aquifers in this area, thus resulting in the compaction of the aquifer sediment (Johnson, Ramage, & Kasmarek, 2011; Kasmarek, Johnson, & Ramage, 2010). Historically, groundwater has been the primary source of water for industrial use, municipal supply, and irrigation, and groundwater use in the HG had sharply increased for a few decades to meet the needs of the rapidly growing population (Seifert & Drabek, 2006). In addition, the complex geologic setting, laterally diverse subsurface hydrological units, regional faults, hydrocarbon extraction, and salt dome movement in HG region (Coplin & Galloway, 1999) have made it difficult to uniquely characterize the source(s) of the observed surface subsidence.

Realizing the significant subsidence over the HG region, the U.S. Geological Survey (USGS), in cooperation with the Texas Legislature, established Harris-Galveston Subsidence District (HGSD) for the purpose of preventing land subsidence in 1975 (HGSD, 2014). Accordingly, a network of discrete borehole extensometers was installed over the HG region to monitor groundwater level changes and measure accumulated clay compaction to better understand the extent and magnitude of the regional subsidence (Kasmarek et al., 2010). Starting in the early

* Corresponding author at: Huffington Department of Earth Sciences, Southern Methodist University, P.O. Box 750395, Dallas, TX, 75275, USA.

http://dx.doi.org/10.1016/j.rse.2015.08.027
0034-4257/

Fig. 1. Shaded relief map of Houston–Galveston, where faults (black lines) (Khan et al., 2014; Khan, 2014), GPS benchmarks (with prefix PAM and marked by blue dots), Extensometers (marked by pink stars), County boundaries and six ground water regulatory areas (by HGSD and FBSD) are superimposed. The ADKS and NETP are co-located extensometer/GPS stations, which are annotated in red. The GPS CORS station NETP is also used as the reference point in this study. The white rectangles represent the coverage of four SAR datasets used in this study. The map of Texas State is an inset on the upper-left corner.

1990s, the HGSD and National Geodetic Survey (NGS) conducted first-order leveling surveys periodically using a combination of Global Positioning System (GPS) survey campaign and quasi-permanent Port-A Measure (PAM) surveys to measure subtle height changes to the land surface elevation (Fig. 1) (Bawden, Johnson, Kasmarek, Brandt, & Middleton, 2012; Kasmarek et al., 2010). Along with collecting data, the HGSD had also outlined the regulations on the groundwater withdrawal across Harris and Galveston counties in 1975 by dividing the two counties into three regulatory areas (Harris-Galveston Subsidence District, 2013a) (Area A, B, and C in Fig. 1). Area A is located in southeastern Harris County reaching Galveston County. The area B is mainly in south-central Harris County covering a small part of Galveston County where the majority of Houston city lies. The area C is situated in the northern and northwestern parts of Harris County. Within the Fort Bend County, the Fort Bend Subsidence District (FBSD) was created in 2003 to provide the regulation on the groundwater extraction; three regulatory areas were formed (see three dissected areas in Fort Bend County of Fig. 1). Due to the regulatory efforts of federal and state authorities, surface deformation in the Houston area, especially over HGSD and FBSD, has also been quantified by using a variety of methods including extensometers, leveling and LIDAR surveys, and so on (e.g., Holzer & Bluntzer, 1984; Kasmarek et al., 2010; Khan, Huang, & Karacay, 2014; Kasmarek, Johnson, & Ramage, 2012). Even though ground-based monitoring techniques and the GPS measurements provide high-accuracy subsidence measurements at discrete locations, they have limitations in providing more detailed and comprehensive information on the ground settlement. In addition, operating these measurement networks in the field is time consuming, labor intensive, and costly. Because the heavy consumption of groundwater under the spatially-variant hydrogeology of the Gulf Coast aquifer can induce significant subsidence over extensive areas in HG, temporally and spatially dense observations are required to understand the complicated characteristics underlying the ground deformation (Kasmarek et al., 2010; Johnson et al., 2011).

Interferometric Synthetic Aperture Radar (InSAR) is a powerful tool for remotely mapping ground deformation caused by land subsidence, landslides, earthquakes, volcanoes, etc. (e.g., Lu & Dzurisin, 2014; Massonnet et al., 1993; Schmidt & Bürgmann, 2003; Zebker, Rosen, Goldstein, Gabriel, & Werner, 1994). In contrast to the ground-based measurements, the satellite InSAR technique has the ability of measuring deformation with a centimeter- to millimeter-level accuracy over a large area. The conventional InSAR method (i.e. Differential InSAR) was applied to investigate land surface subsidence based on individual interferograms (e.g., Amelung, Galloway, Bell, Zebker, & Laczniak, 1999; Bawden, Thatcher, Stein, Hudnut, & Peltzer, 2001; Lu & Danskin, 2001; Peltzer & Rosen, 1995). However, the spatial and/or temporal decorrelation between SAR acquisitions often restricts the robust measurement and thereby the retrieval of reliable ground deformation from the conventional InSAR method (e.g., Zebker & Villaseno, 1992)

and the accuracy of the InSAR measurements can be significantly reduced by the orbital and atmospheric artifacts (Ferretti, Prati, & Rocca, 2001). Accordingly, the multi-temporal InSAR (MTI) techniques, such as Persistent Scatterers InSAR (PSInSAR), Small Baseline Subset (SBAS) InSAR and SqueeSAR, have been developed to map land surface displacements by overcoming temporal/spatial decorrelation and minimizing the artifacts existing in the conventional InSAR (Berardino, Fornaro, Lanari, & Sansosti, 2002; Ferretti et al., 2001, 2009, 2011; Hooper, Zebker, Segall, & Kampes, 2004; Lanari et al., 2004; Lu & Zhang, 2014; Lu, Dzurisin, Jung, Zhang, & Zhang, 2010; Mora, Mallorqui, & Broqustas, 2003; Parizzi & Brcic, 2011; Werner, Wegmuller, Strozzi, & Wiesmann, 2003). The MTI technique has facilitated land subsidence monitoring in many urban areas, such as Las Vegas, USA (Burbey, 2002), Los Angeles, USA (Zhang et al., 2012), Granada, Spain (Joaquim, Hooper, Hanssen, Bastos, & Ruiz, 2011), Naples, Italy (Tesauro et al., 2000); Morelia, Mexico (Cigna et al., 2012), Paris, France (Fruneau & Sarti, 2000), Lisbon, Portugal (Heleno et al., 2011), Hong Kong, China (Ding, Liu, Li, Li, & Chen, 2004), Xi'an, China (Qu et al., 2014), and Shanghai and Tianjin, China (Perissin & Wang, 2010).

The HG region has been studied by multiple researchers using the InSAR technology (Bawden et al., 2012; Buckley, Rosen, Hensley, & Tapley, 2003; Khan et al., 2014; Stork & Sneed, 2002). Stork and Sneed (2002) utilized ERS interferograms spanning 1996–1999 to compare with the patterns of extensometer measurements. Buckley et al. (2003) generated nearly 60 InSAR images spanning 1996–1998 from two neighboring ERS-1/2 tracks. Regional subsidence in the northwestern HG, localized subsidence near Seabrook, and the movements across Long Point fault were observed in their study. Bawden et al. (2012) mapped the spatial extent of the land subsidence over HG from ERS-1/2 images and integrated the InSAR measurements with the HGSD–NGS GPS and extensometer data between 1993 and 2010. Khan et al. (2014) presented PS-InSAR results from 25 ERS scenes during 1992–2002 over a small area of HG. The previous studies identified land subsidence stages in 1992–2002 by either the analysis of individual interferogram based on the conventional InSAR method or PSInSAR over a limited region. In addition, the observed ground displacement signals were mixed with significant noises due to the variations in decorrelation, atmospheric conditions, satellite orbit errors and/or digital elevation model (DEM). New data and more advanced InSAR processing methods are needed to obtain the latest rate, extent, and temporal evolution of land subsidence at the highest spatial density in HG region.

In this study, we utilize a MTI processing method (Hooper, 2007, 2008) to investigate land subsidence over the HG region. By combining both PSInSAR and SBAS approaches, MTI can maximize the spatial density of usable signal, allowing the identification of persistent scatterers (PSs) that dominate the scattering from the resolution element and slowly-varying filtered phase (SFP) pixels whose phases, when filtered, decorrelate little over short time intervals (Hooper, 2008). PS pixels (those contain dominant scatterers) and SFP pixels (whose filtered phases remain adequate coherence) form two distinct, but overlapping sets of pixels used in the MTI analysis. The objectives of this study are to examine the spatial and temporal variability in surface deformation around the HG and to assess the roles that fluid withdrawal (groundwater withdrawal and hydrocarbon extraction), salt tectonics, and faulting play in surface deformation using the MTI technique. All of the available SAR images, including ERS-1/2 (1993–2000), Envisat (2004–2010), and ALOS (2007–2011) datasets, are used to unravel the characteristics of ground deformation from 1993 to 2011. First, time-series deformation from 1993 to 2011 is estimated by integrating C- and L-band MTI measurements to characterize the temporal and spatial variations of land subsidence. Second, GPS and extensometer observations are employed to validate our InSAR time-series results, while cross-validation of MTI-derived deformation measurements from adjacent ERS tracks during 1995–1998 as well as from ascending L-band ALOS and descending C-band Envisat datasets during 2007–2010 is also conducted. Third, a comprehensive annual subsidence rate from 1993 to 2011 is obtained using four InSAR datasets and is correlated with the pattern of ground water withdrawal. Finally, we discuss how the land subsidence in HG is related to groundwater withdrawal, hydrocarbon extraction, salt tectonics, and faulting.

2. Hydrogeologic setting of study area

In Texas, the Gulf Coast aquifer extends from the Rio Grande northeastward to Louisiana along the coastal part of the Gulf of Mexico (Ashworth & Hopkins, 1995) (Fig. 2). More than 1.3 billion m^3 of groundwater is annually withdrawn from this aquifer in Texas (Chowdhury & Turco, 2006; Khan et al. 2014). Baker (1979) identified five hydrological units within the Gulf Coast aquifer system based on their hydraulic and facies properties: the Chicot aquifer (top layer), the Evangeline aquifer, the Burkeville confining layer, the Jasper aquifer, and the Catahoula aquifer (bottom layer). The hydrogeologic cross section AA' (Fig. 2) shows that the classified units dip and thicken from northwest to southeast. The water-bearing units of the Gulf Coast aquifer are composed primarily of horizontally and vertically discontinuous fine-grained to coarse-grained sands and gravels with complex interbedded silts and clays (Ashworth & Hopkins, 1995). The three primary aquifers in the Gulf Coast aquifer system are Chicot, Evangeline, and Jasper (Fig. 2). The Chicot is the uppermost aquifer, consisting of Pleistocene- and Holocene-age sediments. The Evangeline aquifer consists of Miocene- and Pliocene-age sediments while Jaspre aquifer is composed of Miocene-age sediments (Baker, 1979, 1986). The Chicot and Evangeline aquifers are the primary water source. Inexistence of confining unit between the Chicot and Evangeline aquifers (Fig. 2) allows groundwater flow between them. Because of this hydraulic connection, changes in the hydraulic properties of one will affect the properties of the other (Baker, 1979; Kasmarek et al., 2010). The Chicot aquifer can be differentiated from the geologically similar Evangeline aquifer by their hydraulic conductivity (Carr, Meyer, Sandeen, & McLane, 1985) and the position of aquifer outcrops-the Chicot outcrops closer to the coast compared to the Evangeline. The Catahoula aquifer, the bottom layer of the Gulf of Mexico aquifer system (not shown in Fig. 2), has not been exploited for water resource in HG and therefore is not discussed in this study.

Although the lithology of the Gulf Coast aquifer is unconsolidated, normal faulting exists with the Gulf of Mexico basin continues to evolve (Chowdhury & Turco, 2006; Bawden et al., 2012). The faults in the HG region are deep-seated and ancient, and their surficial process can be described as a cut-and-fill scarp and cause damages to buildings and infrastructures (Engelkemeir & Khan, 2008). The strike of faults found in the HG is generally parallel to the coastline (Chowdhury & Turco, 2006). Most of the faults in the Houston metropolitan area are rooted in the subsurface at depths of 975 to 3960 m,have a dip of about 70° (Khan, Stewart, Otoum, & Chang, 2013; Verbeek, Ratzlaff, & Clanton, 1979). These growth faults have throws that increase with depth and strata are thicker on the downthrown side than on the upthrown side. The faults motion does not result in earthquakes, because they are aseismic. The maximum motion rate of the faults is between 1 and 3 cm/yr (Buckley et al., 2003; Shaw & Lanning-Rush, 2005). Three largest fault systems in the HG area are the Long Point Faults system, the Addicks Faults system, and the Hockley Faults system (O'Neill & Van Siclen, 1984). Salt tectonics in the region can also affect the flow of groundwater as well as ground deformation. The Jurassic-age salt was deposited, when the Gulf of Mexico was not fully open to the young Atlantic (Kasmarek & Strom, 2002). The salt penetrates upward through the younger, denser sediments, and nearly reaches the surface in some cases (Jorgensen, 1975).

3. Datasets and processing methods

3.1. GPS, extensometer and water-level measurements

GPS data were obtained by the National Geodetic Survey (NGS) from two types of sites, Continuously Operating Reference Stations (CORS)

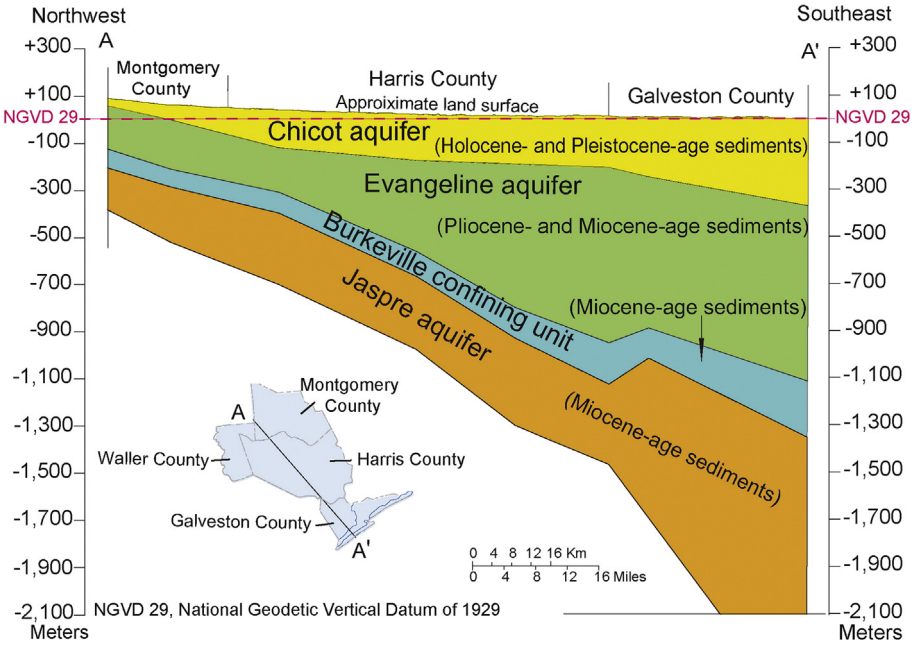

Fig. 2. Hydrogeologic section of the Gulf Coast aquifer system in Harris and adjacent counties, Texas (Baker, 1986; Bawden et al., 2012). (For interpretation of the references to color in this figure legend, the reader is referred to the web version of this article.)

and Port-A Measure (PAM) (Bawden et al., 2012). The NGS reprocessed all available GPS data (CORS and PAM) from January 1, 1993 to December 31, 2009 using the baseline-pair approach. Based on the GPS time-series stability and InSAR analysis in Bawden et al. (2012), NETP station is selected as a reference in the local baseline-pair reference frame, and all regional motions are tracked with respect to this station.

A network of extensometers in HG area was installed and managed by the USGS in partnership with HGSD, beginning in 1973 at selected sites. Extensometer data are used to quantify the rate of aquifer compaction, thereby providing a tool for evaluating the effects on subsidence rates caused by groundwater withdrawal from the aquifers. Borehole extensometers are deeply anchored benchmarks. An inner pipe rests on a concrete plug at the bottom of the borehole and extends to the top. A measurement of the distance from the inner pipe to the surrounding land surface provides the amount of compaction that has occurred, that can be accurately measured and recorded (Harris-Galveston Subsidence District, 2005; Kasmarek et al., 2012). The borehole extensometer measurements at 11 sites in Harris and Galveston Counties are applied to the time-series analysis in this study.

The groundwater level data collected by USGS during 1977 and 2012 are processed to monitor the changes of groundwater level in the aquifer systems. Water-level measurements at wells represent water-level altitudes during the observation periods, and are used to compare the InSAR-derived ground surface deformation.

The locations of principal faults (Fig. 1) mapped by Khan et al. (2014) and Khan (2014) based on airborne LIDAR data are used to study the changes in the observed surface subsidence across the faults. The location map of salt domes obtained from USGS (Huffman, Kinney, Biewick, Mitchell, & Gunther, 2004) is used to discuss the surface deformation due to salt tectonics.

3.2. Available SAR data

The HG region is covered by a total of 29 ERS-1/2 scenes from two adjacent descending satellite tracks 212 and 484, 21 Envisat scenes from descending track 212, and 12 ALOS PALSAR scenes from ascending track 175 (Fig. 1). The radar satellite travels from approximately north to south and looks to the west during the descending track while it travels from south to north and looks to the east during the ascending track. Both ERS-1/2 and ENVISAT SARs operate at C-band (5.7 cm wavelength) while ALOS PALSAR operates at L-band (23.6 cm wavelength). More detailed characteristics on SAR data used in this study can be found in Table 1.

The 1-arc-second (~30 m) Shuttle Radar Topography Mission (SRTM) DEM is used as an external DEM to remove the topographic phase from the interferograms (Massonnet et al., 1993). The precise orbit data provided by Delft Institute for Earth-Oriented Space Research (DEOS) for ERS-1/2 and the DORIS precise orbit data for Envisat satellites are used to improve the accuracy of satellite's positions and interferogram baseline estimates.

3.3. Multi-temporal InSAR algorithm

Conventional InSAR is limited by the spatial and temporal decorrelation between SAR acquisitions, which often makes results less robust (e.g., Zebker & Villaseno, 1992). In addition, the accuracy of InSAR measurements can be significantly reduced by orbital errors and atmospheric artifacts. MTI methods aim at overcoming these limitations. Currently, there are two broad categories of MTI techniques: PSInSAR (e.g., Ferretti et al., 2001) and SBAS (e.g., Berardino et al., 2002). The PSInSAR technique has been successful when applied to urban areas where man-made structures produce efficient reflectors, persistent scatterers (PSs) that dominate background scattering (Ferretti et al., 2001; Hooper et al., 2004). For a resolution element containing no dominant scatterer, phase variations due to decorrelation between observations often obscure the underlying deformation signal. However, by forming interferograms only between images with a short time interval, the temporal decorrelation is minimized. Pixels whose phase values, when filtered, decorrelate little over short time intervals, which are referred as slow varying filtered phase (SFP) pixels, are the targets of SBAS processing (Hooper, 2008). The PS pixels and SFP pixels form two distinct, but overlapping with set of pixels. Therefore, by

Table 1
SAR data characteristics in HG.

Sensor	ERS-1/2		Envisat ASAR	ALOS PALSAR
Band	C		C	L
Polarization	VV		VV	HH, HV
Wavelength (cm)	5.6		5.6	23.6
Track	212	484	212	175
Frame	2997, 3105	2997, 3105	3000	570, 580, 590
Heading (°)	−168.2	−168.2	−165.6	−10.3
Incidence angle (°)	23.1	23.2	23.2	38.7
Number of used scenes	18	12	21	12
Date range (yyyymmdd)	19951216–20001219	19930902–19971109	20050129–20100925	20070926–20110104
Number of measurement pixels	867,605	555,440	1,506,445	5,259,788

combining both PSInSAR and SBAS approaches the spatial density (both PS and SFP pixels) of usable signal could be maximized.

3.3.1. PSInSAR processing

The PSInSAR technique utilizes a time series of radar images to detect coherent PS points in the study region. A master image is chosen from the available SAR images based on favorable geometry related to all other images, high coherence and possibly minimum atmospheric disturbances. After the coregistration between master and slave images, a series of interferograms are constructed using of precise orbit information. The main idea of PSInSAR is to discern coherent radar signals at PS from incoherent contributions in order to obtain physically meaningful observations. In this work, StaMPS (Stanford Method for Persistent Scatterers) is used for PSInSAR processing (Hooper et al., 2004). StaMPS uses both amplitude and phase analyses to determine the probability of PSs at individual pixels. An initial selection based on amplitude analysis is performed at first (Ferretti et al., 2001), and then the phase analysis is used to refine the PS probability by an iterative process (Hooper et al., 2004; Hooper, Segall, & Zebker, 2007). The spatially-correlated phase components of the interferometric phase at a PS candidate pixel, including the ground displacement, the orbital inaccuracy, the temporal change in atmospheric delay and the spatially-correlated height error, are estimated by a frequency-domain adaptive band-pass filter of surrounding pixels. The spatially-uncorrelated phase contributions, including both the deviation of the pixel's effective phase center from its physical center (i.e., spatially-uncorrelated look angle error) and the spatially-uncorrelated height error, are then estimated through their correlation with the perpendicular baseline. Subtraction of the two estimates (i.e., the spatially-correlated and spatially-uncorrelated terms) from the interferometric phase leaves an estimate of the decorrelation noise, γ_x. γ_x represents the variations in the residual phase at the PS candidate pixel (Hooper, 2008; Hooper et al., 2004, 2007):

$$\gamma_x = \frac{1}{N}\left|\sum_{i=1}^{N} \exp\left\{\sqrt{-1}\left(\psi_{x,i} - \Delta\psi^{u}_{\theta,x,i} - \tilde{\psi}_{x,i}\right)\right\}\right| \quad (1)$$

where N is the number of interferograms, $\psi_{x,i}$ is the wrapped phase of pixel x in the ith interferogram, $\psi^{u}_{\theta,x,i}$ is the estimate of the spatially-uncorrelated look angle error term and $\tilde{\psi}_{x,i}$ is the estimated spatially-correlated term. The root-mean-square change on γ_x (Eq. (1)) is calculated each iteration. When the change ceases to reduce, the solution has converged and the iteration stops. A threshold value of γ_x, which is determined by the maximum acceptable percentage of misidentified PS pixels, is applied for the selection of final PS pixels. More details about the way that StaMPS identifies PS from interferograms can be found in Hooper et al. (2004, 2007) and Hooper (2008).

3.3.2. SBAS processing

A SBAS method seeks to minimize the separation in both baseline and Doppler frequency of SAR pairs, in order to maximize the interferogram correlation. We select image pairs whose perpendicular, temporal and Doppler separations are below given threshold values based on the data availability and the expected rate of decorrelation, while ensuring no isolated clusters within the resultant network of image-pairs (Hooper, 2008). The interferograms are formed by recombination of the resampled single-look-complex images from the PS processing. Interferograms are filtered in range to reduce the effect of geometric decorrelation and in azimuth to exclude non-overlapping Doppler spectrum. Computational burden is reduced by selecting a subset of candidate pixels through analysis of amplitudes (Hooper, 2008, Hooper et al., 2004). SFP pixels are then identified among the candidate pixels in same way as for PS pixels (Hooper, 2008). SFP pixels are then identified among the candidate pixels through SBAS processing (Hooper, 2008). Note, PS pixels are selected based on single-master interferograms with no spectral filtering in PS processing while SFP pixels are chosen based on multiple-master small-baseline interferograms with spectral filtering in SBAS processing.

3.3.3. MTI processing

The PS and SFP datasets are combined before phase unwrapping to maximize the reliability of the unwrapped phase. In order to achieve this, we calculate the equivalent SBAS interferogram phases for PS pixels by recombining the corresponding single-master interferogram phases (Hooper, 2008),

$$\psi^{SB}_{x,i} = W\left\{\psi^{SM}_{x,s} - \psi^{SM}_{x,m}\right\} \quad (2)$$

where $\psi^{SM}_{x,s}$ is the single-master phase for the SBAS slave, $\psi^{SM}_{x,m}$ is the single-master phase for the SBAS master, and $W\{\bullet\}$ is the wrapping operator. A combined dataset of SBAS interferogram phases can be created from both PS and SFP pixels. A weighted mean value for the phase is calculated by summing the phases from both datasets when a pixel is involved in both datasets. The signal-to-noise ratio (SNR) from each data set is estimated as the weight during the averaging.

$$SNR = \frac{1}{\gamma_x^{-1} - 1} \quad (3)$$

It should be noted that "PS" from now on will be used as the name of the combined sets of PS and SFP pixels for simplicity. The processing of multiple acquisitions together offers the potential to unwrap the phase more robustly in three dimensions (3D) with time as the third dimension (Hooper & Zebker, 2007). There are more potential paths to choose from, which in return decreases the chances of disconnected regions.

3.3.4. Time series inversion

We estimate the spatially correlated error term (including atmospheric artifact and baseline error) by high-pass filtering of the unwrapped phase data in time then low-pass filtering in space (Hooper et al., 2004). Subtracting the estimated error term from the

phase of each PS leaves just the deformation signal and spatially uncorrelated error terms that can be modeled as noise. The unwrapped phases of the SBAS interferograms are then inverted to form a time series of phase at each pixel. As there are no isolated clusters of interferograms, we invert the unwrapped phase in a least-squares method. The retrieved phase is then the phase of each pixel relative to a user defined reference pixel and the master image (reference time).

We construct a total of 181 interferograms including 59 for PS processing and 122 for SBAS processing (Fig. 3). Some interferograms with spatial/temporal baselines larger than the thresholds are also included to guarantee temporal continuity for time-series analysis (Fig. 3). The Doris software (Kampes, Hanssen, & Perski, 2003) is applied for the interferometry processing. Slave images are resampled to the master geometry and corrected for the difference in position of the master and slave sensor, using the WGS84 reference ellipsoid. The four datasets were then processed using the above StaMPS MTI method (both PS and SBAS) respectively.

4. Results and analyses

4.1. Mean deformation rate during three observation periods

We process SAR images from 4 different datasets (Table 1) independently using the MTI processing, and generate line-of-sight (LOS) deformation rate maps over the HG region for the following observation periods: 1995–1998 (ERS; Fig. 4a), 2005–2010 (Envisat; Fig. 4b), and 2007–2011 (ALOS PALSAR; Fig. 4c). The long-term mean deformation rate map during 1995–1998 is calculated by averaging and mosaicking measurements from two adjacent ERS tracks (Fig. 4a). At least two broad-scale subsidence zones can be detected (Fig. 4). The primary large-scale subsidence cone, referred to as the northwestern Harris subsidence field (NWH hereinafter), covers the region of more than 70 km by 40 km elongated northwestward. The subsidence zone spans from Spring (SPR in Fig. 4a) in northern Harris County, through Jersey Village (JSV in Fig. 4a) in Harris County, to Mission Bend (MB in Fig. 4a) over the southwestern bound of Harris County. The maximum

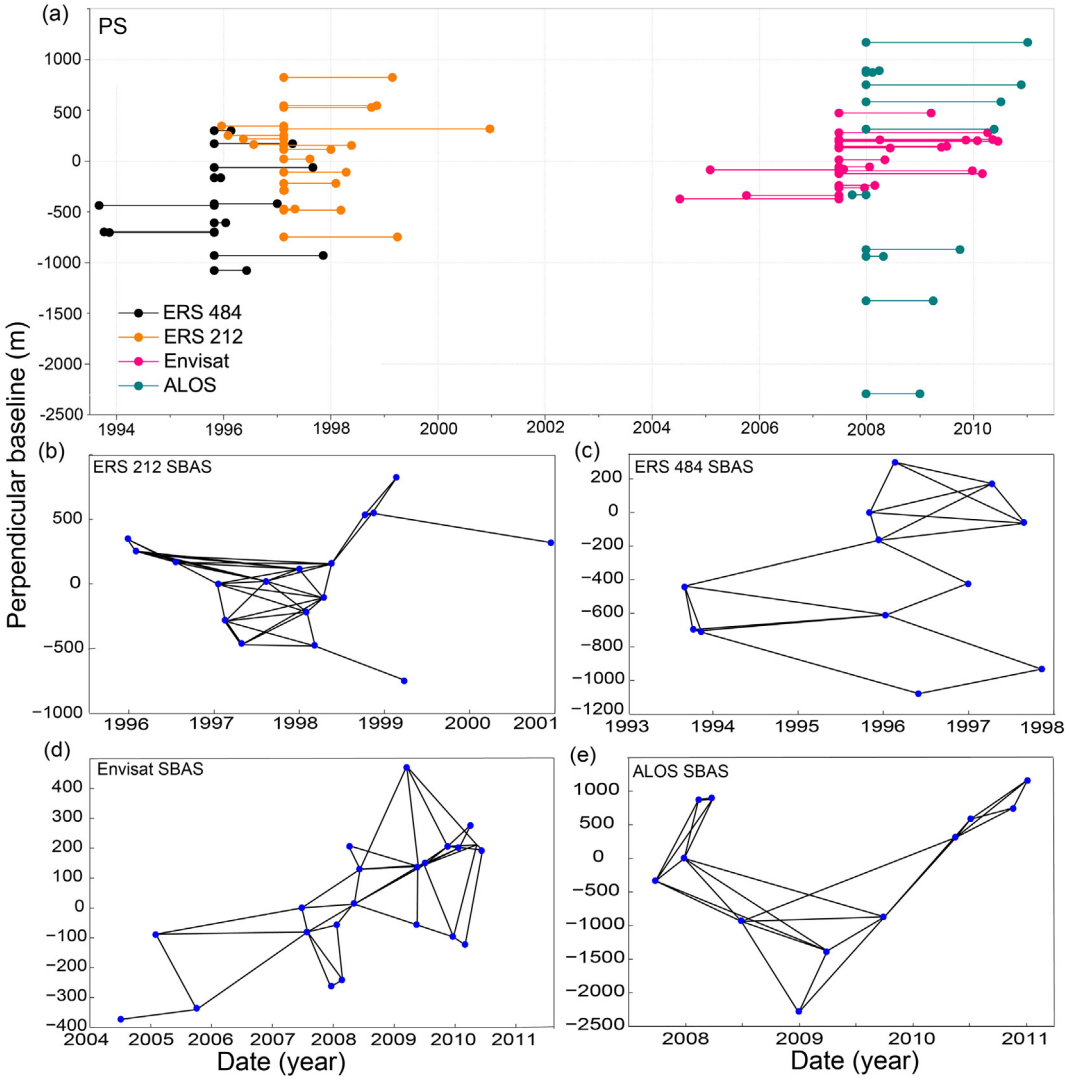

Fig. 3. Temporal–spatial baseline distributions of SAR interferograms of four datasets: (a) PS interferograms: black segments represent 11 interferograms generated by ERS path 484, with 19951105 as the master image; orange segments show 17 interferograms generated by ERS path 212, with 19970114 as the master image; pink segments display 20 interferograms generated by Envisat data, with 20070626 as the master image; navy segments indicate 11 interferograms generated by ALOS data, with 20071227 as the master image; (b–e) SBAS interferograms with perpendicular baselines less than 250 m and temporal baselines less than 400 days for C-band data, and perpendicular and temporal baseline thresholds of 1200 m and 350 days for L-band ALOS data, including 36 interferograms generated by ERS path 212, 20 interferograms generated by ERS path 484, 39 interferograms generated by Envisat, and 27 interferograms generated by ALOS data sets.

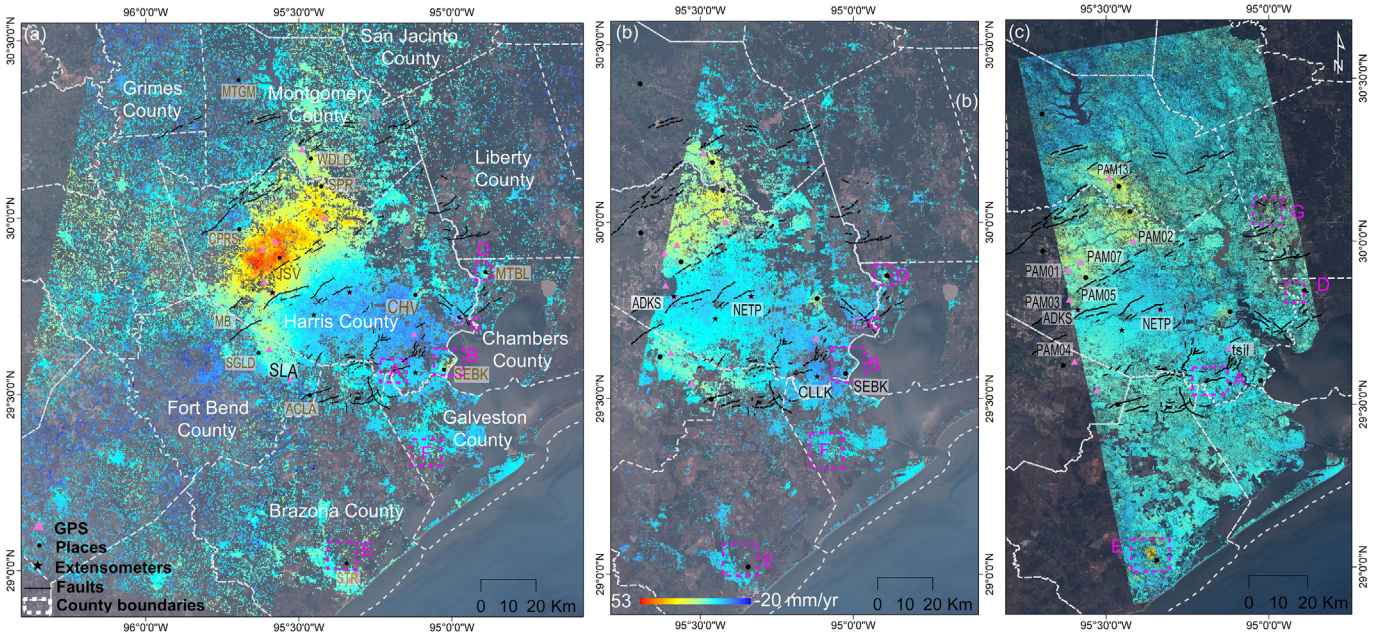

Fig. 4. Annual LOS deformation maps derived from (a) ERS (data period: 1995–1998), (b) Envisat (2005–2010) and (c) ALOS (2007–2011) datasets. The ERS map is a mosaic of two ERS tracks 212 and 484. The main deformation zones and county names are marked on (a) in black ("NWH" and "SLA"). The dark orange marks on (a) (e.g. "JSV") represent major subsidence peaks over the Houston–Galveston region, where the black dots represent their locations (a, b and c). Part of the borehole extensometers and GPS stations are also marked as pink triangle and black stars on (a, b and c), whose names are labeled on (b and c) respectively. The pink boxes in (a, b and c) indicate areas used for the discussion of our InSAR results in Section 5. The colored points from blue to red represent the InSAR values. The cold colors (blue to yellow) represent uplift (negative values) to low-rate subsidence (positive values), and the hot-colored (yellow to red) points show high-rate subsidence in the study area. (For interpretation of the references to color in this figure legend, the reader is referred to the web version of this article.)

subsidence over NWH region is centered between the cities of Jersey Village (JSV in Fig. 4a) and Cypress (CPRS in Fig. 4a). The subsidence rates varied from 10 mm/yr to 53 mm/yr in 1990s and decreased to 10 mm/yr–30 mm/yr after 2000 (Fig. 4). The other large-scale subsidence feature is located to the south of the NWH and is referred as the Sugar Land-Arcola subsidence field (SLA hereinafter). The subsidence zone is elongated northwestward, extending from about Mission Bend (MB in Fig. 4a) through Sugar Land (SGLD in Fig. 4a) to Arcola (ACLA in Fig. 4a). The subsidence rate over SLA area shows relatively lower and more stable values of 20–30 mm/yr between 1993 and 2011. Although rates vary with locations, the signs of uplift are observed in the southeastern Harris County (up to 20 mm/yr) during the whole timespan. Even within this uplift area, localized subsidence can be spotted at many location, including three significant features with an average subsidence rate about 20 mm/yr in Seabrook (SEBK in Fig. 4a), Mont Belvieu (MTBL in Fig. 4a), and Channelview (CHV in Fig. 4a).

Subsidence rates vary both temporally and spatially. During 2004–2011, the maximum rates of subsidence over NWH appear to be decreasing to 20–30 mm/yr compared to that in 1990s, which could be evidenced by both Envisat and ALOS results (Fig. 4b and c). Our MTI results indicate that the extent of subsidence over NWH was shrinking and migrating toward the northeast after 1998 (Fig. 4). The maximum subsidence centers transferred from JSV during 1990s to Spring in Harris County (SPR in Fig. 4a) and The Woodlands (WDLD in Fig. 4a) in Montgomery County after 1998, where a generally steady subsidence rate of 30 mm/yr has been observed during the whole timespan.

4.2. Time series deformation

We have generated time-series deformation maps using MTI to study the evolution of land surface deformation over the HG region. MTI-derived time-series deformation measurements at 12 PS locations are compared with observations from borehole extensometers and GPS stations (Fig. 5). Time-series deformation plots at other GPS stations and borehole extensometers can be found in the Supplementary Data. We select the PS points that lie within 100 m of benchmarks and average displacement values around benchmarks to compare the InSAR-derived time-series displacements with those from GPS and extensometers. After both types of measurements are referenced to the same location and corrected for the offsets in time, we have GPS, extensometers, and InSAR observations in the same temporal and spatial reference frame (Fig. 5).

The main subsidence cones are located at NWH area in northwestern Harris (Fig. 4), all of which experienced subsidence during the observation time span. The rate of subsidence reached the maximum value of about 50 mm/yr at PAM01 during 1994–2003, and decreased to 30 mm/yr after 2003 (Fig. 5a). Similar subsidence trends are observed at the stations PAM03, PAM05, PAM07, and ADKS, all of which are located at southwestern NWH subsidence field (Fig. 5a, c, e, f and i). This is particularly evident at PAM03, PAM05, and ADKS stations that are located at the southern edge of the NWH area, and the subsidence rate decreased up to one-quarter of that before 2003 at each of these stations. The land subsidence at northern NWH (PAM02, PAM13) presented a steady subsidence rate of nearly 30 mm/yr during the whole period. A steady subsidence rate of 20 mm/yr (Figs. 4 and 5d and g) could be observed over the SLA area, which is lower than that at NWH. The CORES station TISL at the southeastern Harris County, on the other hand, observed a ~20 mm/yr uplift during the period of 1993–2011. Overall, subsidence in HG region exhibits temporal–spatial variations during 1993–2011. Even though the ongoing subsidence in the NWH area can be clearly seen from Figs. 4 and 5, the subsidence rate decreased by half from 1993 to 2011. The distribution of land subsidence has gradually migrated to the northeast, and most of the subsidence zones generally agree with the groundwater withdrawal contours (see discussion later).

Comparing InSAR, GPS, and extensometer measurements provides further insights into the source depth of the observed subsidence. Two extensometer sites used for this report were constructed with co-located GPS antennas mounted to the pipe casing. The extensometers measure aquifer system compaction between 6 m below the land surface and the bottom of the borehole, i.e. the top of the Burkeville

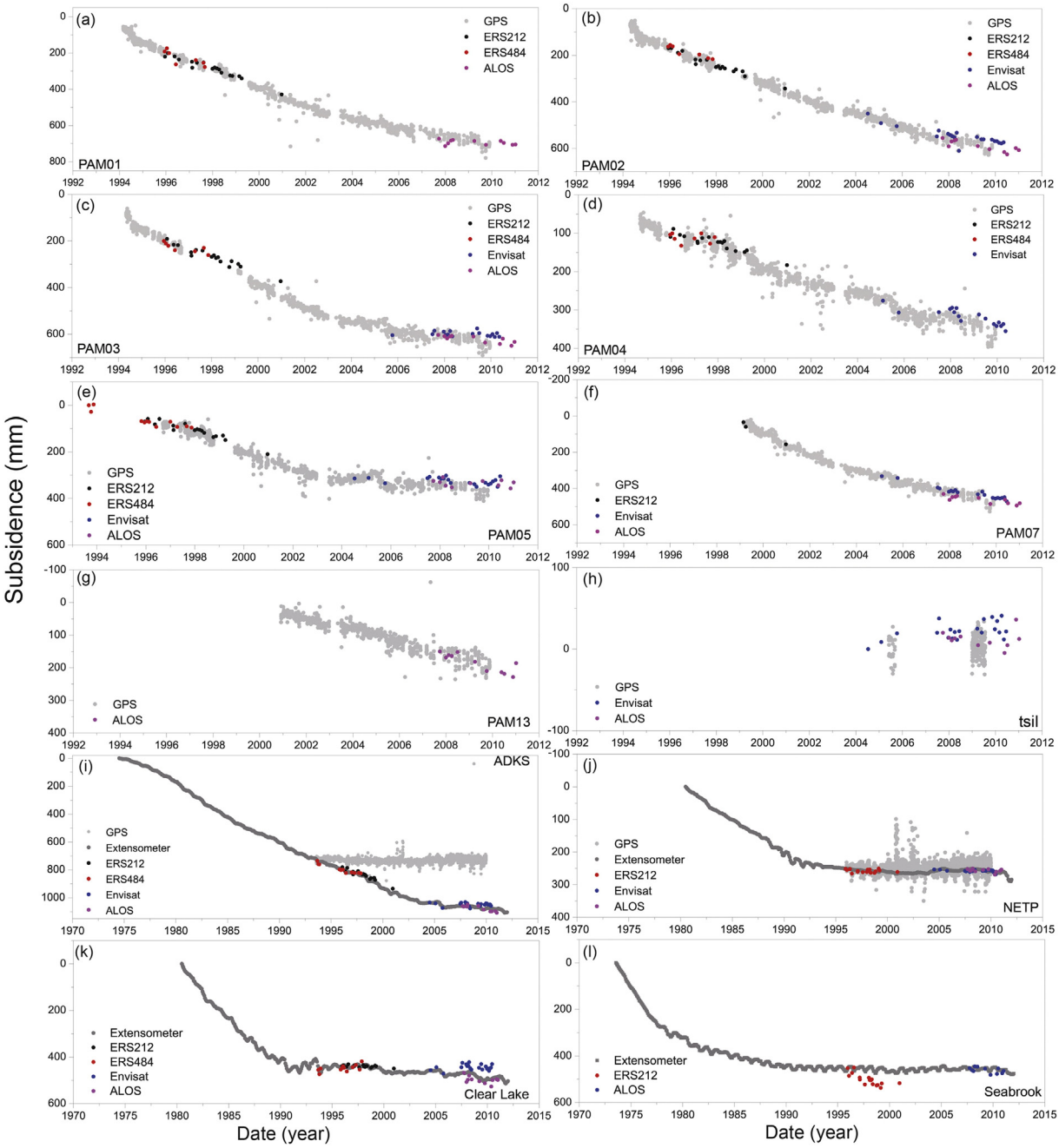

Fig. 5. Comparison of InSAR-derived land surface deformation with those from GPS and extensometers measurements: (a–h) Comparison between InSAR-derived time series subsidence and GPS observations at 8 stations; (i, j) Comparison of InSAR displacement with GPS and borehole extensometer observations at ADKS and NETP stations. (k, l) Comparison of InSAR displacement with borehole extensometer observations at Clear Lake and SW Houston station.

confining layer (549 m deep) at ADKS (Fig. 5i) and the bottom of the Evangeline aquifer (661 m deep) at NETP (Fig. 5j), while the GPS measure the vertical displacement at the bottom of the borehole (Kasmarek et al., 2012; Wang, Yu, Kearns, & Ortega, 2014; Yu, Wang, Kearns, & Yang, 2014). The GPS vertical time-series data at these two sites have indicate little to no vertical motion at the bottom of the extensometer boreholes while coincident extensometer measurements indicate about 400 mm and <20 mm of vertical deformation at sites ADKS and NETP, respectively (Fig. 5i and j). The InSAR measurements used in this study match well with extensometer, so we conclude that the deformation at ADKS and NETP is attributed to the compaction of shallow aquifers (i.e. Chicot and Evangeline). There was no significant vertical motion detected below 661 m deep.

4.3. Accuracy assessment of InSAR results

We first compare the MTI-derived surface deformation measurements using independent InSAR observations that cover the same area and span the same time interval. For the time interval of 1995–1998, we have obtained the mean deformation rate maps from two descending ERS-1/−2 tracks 484 and 212, which overlap by about 25 km in swath (Fig. 1). So the MTI results from these two independent datasets can be used to cross-validate the precision of our MTI measurements. For the period of 2007–2010, we have independent InSAR measurements from Envisat and ALOS (Fig. 1). In order to compare the vertical displacement rates from these dataset, we calculate 2 new mean deformation rate maps spanning approximately 1995–1998 from 2

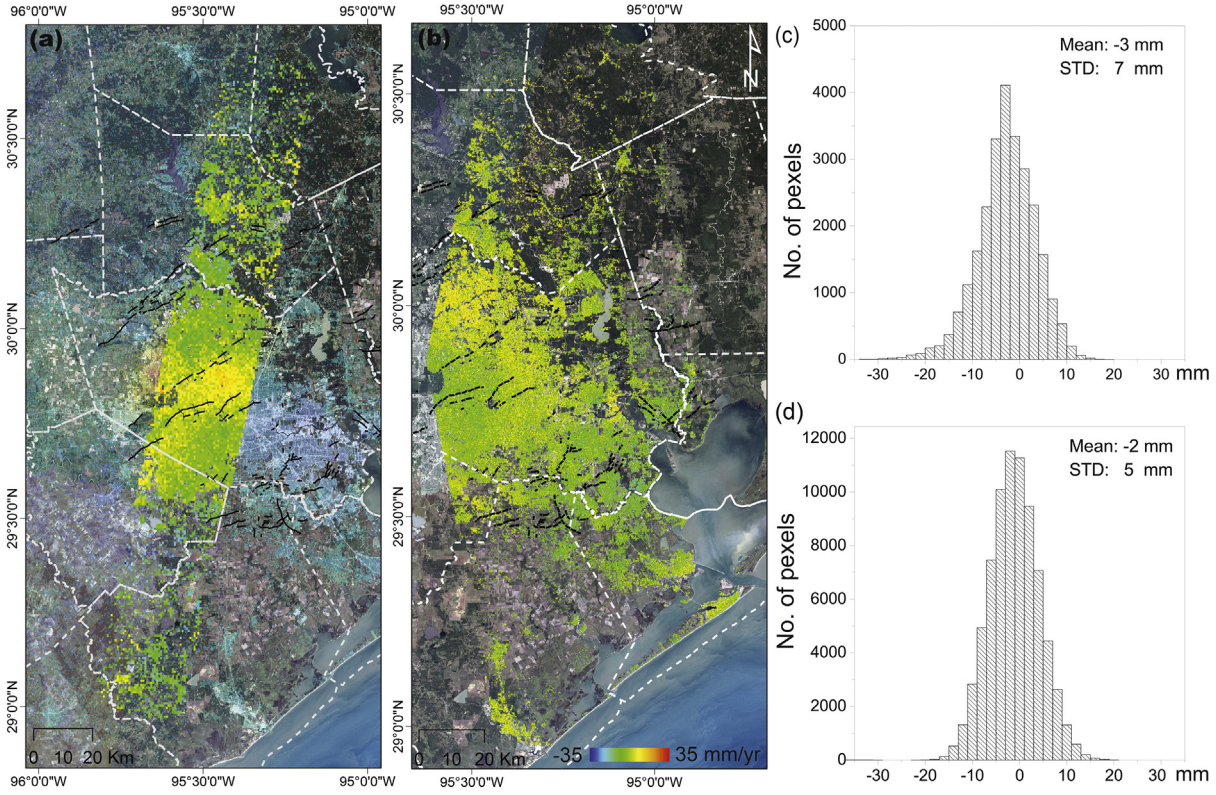

Fig. 6. (a) Difference in the vertical displacements derived from ERS path 212 and ERS path 484 (assuming the observed deformation vertical). (b) Difference in the vertical displacements derived from ascending ALOS and descending Envisat (assuming the deformation vertical). (c) The corresponding histogram of (a). (d) The corresponding histogram of (b).

descending ERS tracks and 2 new mean deformation rate maps spanning 2007–2010 from ALOS and Envisat images. Assuming that the deformation is purely vertical, all four SAR LOS measurements are projected into the vertical direction with respect to the corresponding incidence angles. Then, the overlapped parts of the displacement maps that span the same time interval are selected to compare the vertical deformation measurements between two independent measurements. Fig. 6a shows the difference in vertical displacement from two adjacent ERS tracks. The standard deviation of the difference map is about 7 mm (Fig. 6c). Fig. 6b shows the difference in the vertical displacement from the Envisat and ALOS datasets. The standard deviation is between these two datasets is about 5 mm (Fig. 6d).

We next use continuous GPS measurements to evaluate the results of the land surface deformation from MTI (Fig. 5a–h) by assuming that the deformation is purely vertical. The GPS measurements and the InSAR time-series agree both in the trend and the value (Fig. 5a-j). The average root mean square error (RMSE) of the differences between InSAR and GPS measurements is 10.6 mm, indicating a good agreement between InSAR-derived time series deformation measurements and daily/monthly GPS solutions. Discrepancies at a few benchmarks are likely due to two factors. First, GPS measurements at the exact SAR image dates are not available, so the interpolated time-series deformations of GPS are used to compare with InSAR measurements. Second, InSAR measurements from 4 different imaging geometries are used in the comparison based on the assumption of the purely vertical deformation, which is not completely true for HG. We finally utilize the precise extensometer data (Kasmarek et al., 2010, 2012) to evaluate our InSAR results (Fig. 5i-l). The InSAR-derived time-series deformation measurements show good agreements with those from the extensometers, with a RMSE of 11.7 mm, which is calculated based all available sites in Fig. 5 and the figure in the Supplementary Data. The RMSE between InSAR and extensometer measurements is slightly larger than that between InSAR and GPS, because extensometer observations are conducted monthly and do not reflect the vertical motion below the anchor of installed devices.

5. Characterizing regional land subsidence

Land subsidence can be induced either by one or a combination of several different anthropogenic activities that involve large volume extraction of underground reservoirs (water, hydrocarbons, sulfur, and salt) or by the natural process of sediment compaction, tectonics, and gravity driven process. Extensive subsidence has increased the frequency of flooding, caused extensive damage to infrastructure, roads, reservoirs, and surface-water distribution facilities, and resulted in substantial loss of wetland habitat. Land loss associated with subsidence is common, especially where large volumes of fluids are removed from underground formations. This induced subsidence has its greatest effect on the flat coastal plains and wetlands where minor lowering of the land surface results in permanent inundation (Coplin & Galloway, 1999). In this section, we will explore the correlation of subsidence with groundwater withdrawal, hydrocarbon exploration, salt domes and fault activity in HG area.

5.1. Correlation between land subsidence and groundwater withdrawal

Groundwater withdrawn from the Chicot, Evangeline, and Jasper aquifers has been the primary source of water for municipal supply, industrial and commercial use, and irrigation in the HG region since the early 1900s (Kasmarek & Robinson, 2004). The primary source of the land surface subsidence in the Houston area is attributed to the long-term withdrawal of subsurface fluids (Coplin & Galloway, 1999; Gabrysch & Bonnet, 1975; Pratt & Johnson, 1926). Most of the freshwater supply wells are drilled to the depth of 305–710 m in the Chicot and Evangeline aquifers, where lowering pumping-well water levels leads to the compaction of the fine-grained clay layers within the

aquifer (Gabrysch, 1984; Gabrysch & Bonnet, 1975; Holzer & Bluntzer, 1984; Kasmarek et al., 2010).

The HGSD established a policy in 1975 that gradually decreased the volume pumped throughout its regulatory areas (Fig. 1) with the InSAR, GPS, and extensometer data tracking the temporal and spatial subsidence patterns in response to HGSD regulations. The groundwater withdrawal at regulatory areas (Fig. 1) has been decreased due to the effort of HGSD. The groundwater extraction in Regulatory Area A reduced from 140 million gallons per day (MGD) in 1976–1991 to 10 MGD in 1991 and remained at 10 MGD afterwards. In Regulatory Area B, ground water extraction sharply decreased from 160 MGD in 1976 to 26 MGD in 2012. Groundwater withdrawal in Regulatory Area C reached the maximum value of 270 MGD in 2000, but slightly decreased to about 198 MGD in 2012 (Harris-Galveston Subsidence District, 2013b).

InSAR-derived deformation rates are compared with the spatially varied groundwater level changes, based on both the Chicot and Evangeline aquifer wells, to highlight the correlation between the subsidence and the groundwater level change throughout the study area. Fig. 7a and b show the average deformation rate from 1993 to 2011 based on both C- and L-band InSAR measurements over the study area. Comparisons between the annual surface deformation and the groundwater level changes during the periods of 1977–2012 and 1990–2012 are conducted, respectively (Fig. 7a and b). The correlation between the land subsidence and ground- the water level declines is high with a correlation value of about 0.8. The scatter plots in Fig. 7c and d show the correlation between the ground water level change and the subsidence rates. We use a linear regression to describe the variation of the subsidence with the water level change. The coefficient of determination, R^2 for the two linear regressions are about 0.81 and 0.53, respectively. Better agreement comes from the comparison between the average deformation rate and the 1977–2012 groundwater level change. This suggests a delayed effect on aquifer compaction due to ground water withdrawal as what has been observed in previous study (Kasmarek et al., 2012; Yu et al., 2014). Groundwater withdrawals decreased significantly within Regulatory Areas A and B (Fig. 1) after 1976. The groundwater levels at almost all extensometer sites rose during the past four decades. As a result, the rates of aquifer compaction have decreased, even slightly rebounded at some sites since 1990, about 15 years after the regulation of groundwater withdrawal. Rates of groundwater withdrawal have sharply dropped since 1976, leading to the decrease of pore pressure and the relaxation of the sediment

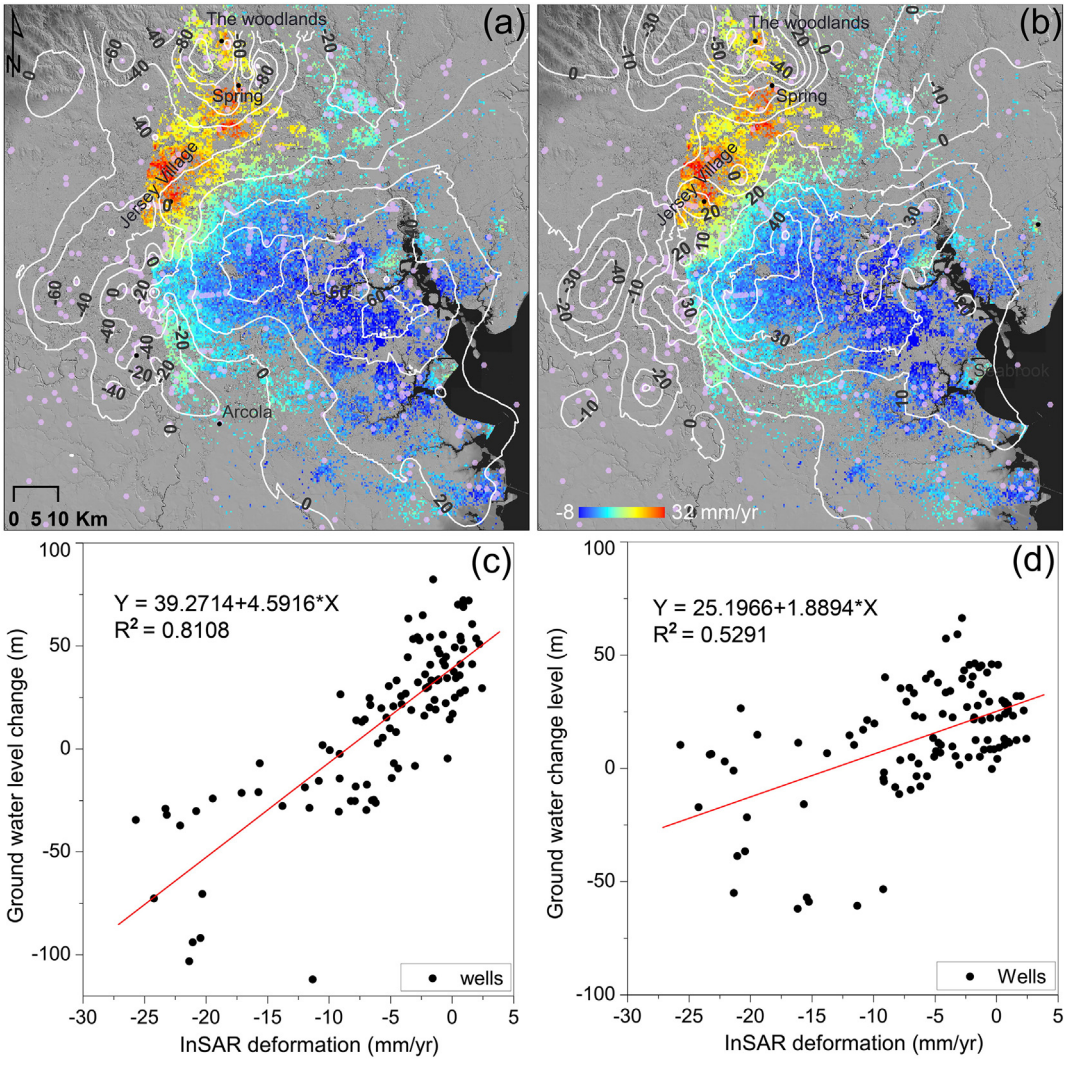

Fig. 7. Annual deformation rate during 1993–2000 along with contours of groundwater level changes at both Chicot and Evangeline aquifers for the periods (a) 1977–2012 and (b) 1990–2012. The contour line colors from orange dark (negative value) to light (positive values) represent ground water level changes from decline to rise. The purple dots in (a) and (b) display the locations of water wells used to derive the contours. (c) Correlation between the groundwater level change from 1977 to 2012 and the InSAR annual deformation rate during 1993–2011; the red line is linear regression of these wells. (d) Correlation between the groundwater level change from 1990 to 2012 and the InSAR annual deformation rate during 1993–2011; the red line is linear regression of these wells. (For interpretation of the references to color in this figure legend, the reader is referred to the web version of this article.)

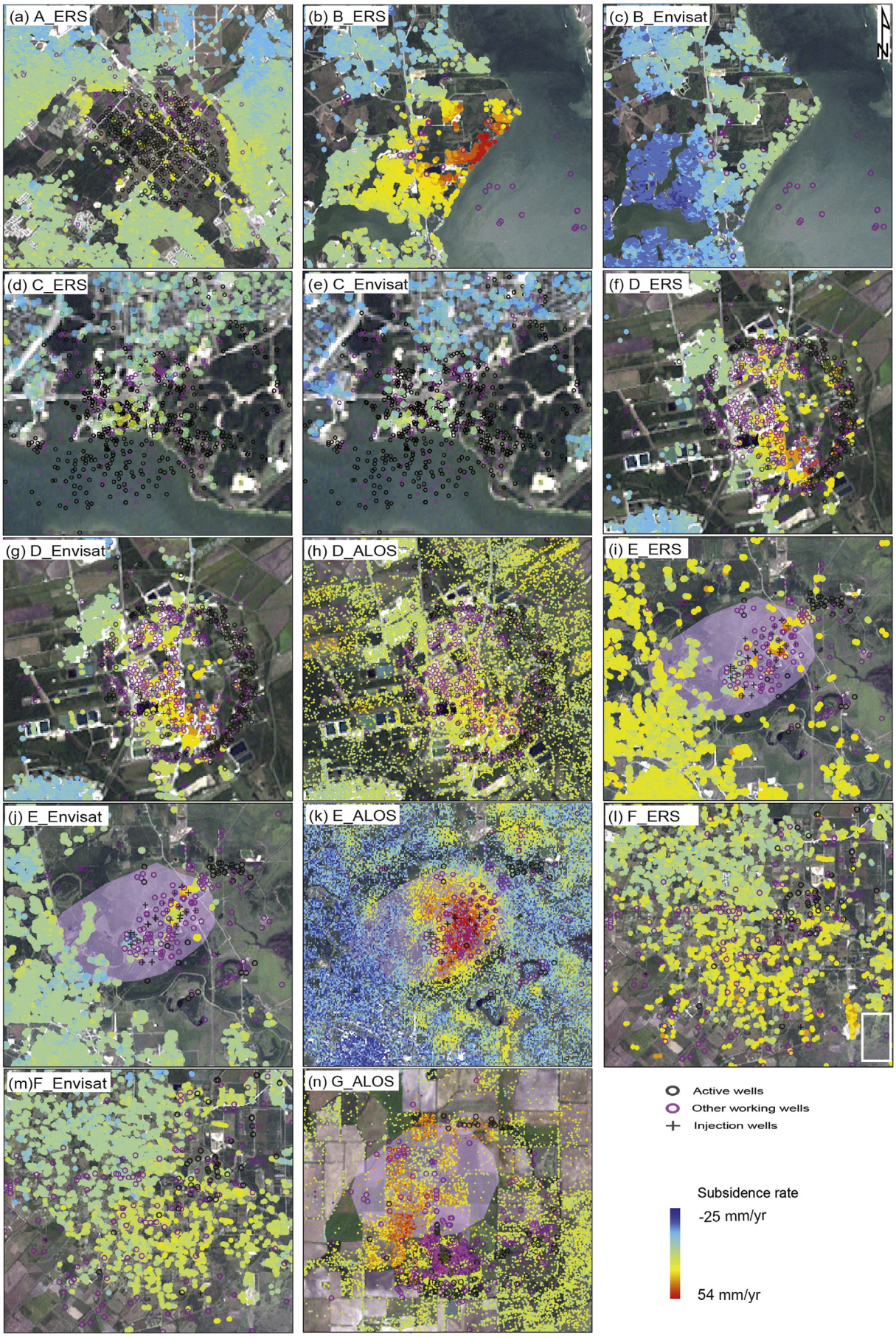
(a) A_ERS
(b) B_ERS
(c) B_Envisat
N
(d) C_ERS
(e) C_Envisat
(f) D_ERS
(g) D_Envisat
(h) D_ALOS
(i) E_ERS
(j) E_Envisat
(k) E_ALOS
(l) F_ERS
(m)F_Envisat
(n) G_ALOS
Active wells
Other working wells
Injection wells
Subsidence rate
-25 mm/yr
54 mm/yr

compression (Kasmarek et al., 2012). As a result of this, the subsidence rate has declined significantly.

The contour maps of groundwater level changes reaffirm that the subsidence feature has been moving toward the northeast during the past decades (Fig. 7a and b). The subsidence at Regulatory Area A, including Galveston, downtown Houston and, coastal areas has been nearly stabilized (<10 mm/year). Subsidence greater than 10 mm/year and up to 30 mm/year is still ongoing at northwestern HG, including Spring, Jersey Village, Addicks, and the Sugar Land area. These areas are located in Regulatory Area C of the HGSD regulation plan (Harris-Galveston Subsidence District, 2013a, b) or Regulatory Area A of the 2013 FBSD regulation plan (Fort Bend Subsidence District, 2013), where new groundwater regulation went into effect in 2010. Groundwater drawdown has ceased in most of the HG area but continues in northwestern and western Harris County and northern Fort Bend County. Surface uplift has been observed at all of the wells at the eastern HG in response to the elevated groundwater levels. Therefore, the general uplift in the eastern HG is mainly due to the groundwater recovery (Fig. 7). The good correlation between InSAR deformation and groundwater level can attest that groundwater withdrawal exerts significant control on the overall subsidence throughout the study area. Local variations in surface deformation are due to spatial variations in the amount of the water withdrawal as well as fine-grained deposits in the aquifers as observed elsewhere (e.g., Lu & Danskin, 2001).

5.2. Local land subsidence caused by hydrocarbon exploration

Even though the groundwater extraction is a key driver in land subsidence over HG area, oil and gas exploration and related production activities have also contributed to the localized subsidence. Pressure relief in oil/gas production sites can lead to reservoir compaction, movement of the overburden, and land surface deformation above/within the reservoir. The first recognized ground deformation associated with oil/gas fluid withdrawal was in the vicinity of the Goose Creek Oil Field (Pratt & Johnson, 1926). The subsidence of overlying terrain was definitively attributed to the extraction of petroleum based on the fact that the subsidence occurred before major water-level declines began (Holzer & Bluntzer, 1984). By using leveling profiles, Holzer and Bluntzer (1984) detected 6 hydrocarbon exploration fields as local subsidence cones and 4 hydrocarbon exploration fields with substantially lower subsidence rates than the surrounding area (i.e. relative uplift) during 1910s and 1970s. We have found only three oil fields were active during the time span of available InSAR data: Goose Creek, Barbers Hill, and Humble oil fields. Our InSAR results confirm continuing deformation over these fields (Fig. 8c–h). The Goose Creek field (area C in Fig. 4) is located along the northern shoreline of Galveston Bay, where Goose Creek exits to the sea. Subsidence over the Goose Creek field is particularly dramatic and well documented (Holzer & Bluntzer, 1984; Pratt & Johnson, 1926). The field, that were once above water, are now wholly or partially inundated, and the area of subsidence almost exactly meets at the boundary of the productive region. There are dense areas of wells drilled for multiple uses. Both ERS and Envisat data have shown a 5–10 mm/yr localize subsidence feature over the dense active wells area (Fig. 8c and d). This data indicates that the subsidence revealed in previous studies (Holzer & Bluntzer, 1984; Pratt & Johnson, 1926) is continuing through 2011, which was mainly due to petroleum extraction. Barbers Hill (D in Fig. 4) is another active field, where a large number of production units are located. Our InSAR results from 3 independent datasets indicate a subsidence of more than 20 mm/yr centered at the southwestern part of the oil field, where a large amount of active wells are distributed but fewer injection wells (Fig. 8f, g, and h). This contrasts to the observed uplift over the oil field before 1970 (Holzer & Bluntzer, 1984). Even though Holzer and Bluntzer attributed the relative uplift at Barbers Hill to salt dome activity, we can conclude that the present state of subsidence since 1993 was likely caused at least in part by hydrocarbon exploration. The Humble oil field, an oil-producing area located about 2 km northeast of the town of Humble in northeastern Harris County, is the third most active field. The Humble oil field has drawn negligible amount of oil and gas from the anhydrite and limestone reservoir on the caprock and the flanks of a salt dome at the depths of 180 to 1780 m (Smith, 2010). The deformation at Humble oil field presented a relative uplift with respect to the surrounding areas (Holzer & Bluntzer, 1984). Detailed discussion will be conducted at the next section for its complexity.

Our InSAR-derived deformation maps allow us to discover 5 new subsidence cones centered at hydrocarbon production fields: Webster (A in Fig. 4), Seabrook (B in Fig. 4), Stratton Ridge (E in Fig. 4), Santa Fe (F in Fig. 4) and North Dayton (G in Fig. 4). Generally, the locations of the subsiding areas correspond to the distributions of working wells (Fig. 8). A localized subsidence feature has been mapped at the Webster oil field (Fig. 8a), where petroleum was discovered in the 1930s. No considerable subsidence was found before 1980s (Holzer & Bluntzer, 1984). Our InSAR results indicate that subsidence occurs at a rate of 15 mm/yr during 1990s, and the spatial extent of the subsidence corresponds to the distribution of active wells (Fig. 8a).

One of the more significant results of the InSAR analysis comes from the detected subsidence over the Seabrook oil filed (Fig. 8b and c). As discussed briefly at an earlier section, a discrepancy in observed surface deformation between InSAR and extensometer time series data at the Seabrook station during 1995 and 2000 can be found in Fig. 5l. The extensometer is located at the bottom of Chicot Aquifer at depth of 420.9 m. During 1990 and 2011, the compaction measurement at the Seabrook borehole extensometer shows little to no deformation while InSAR measures subsidence at a rate ranging from 10 to 30 mm/yr (Fig. 5l). The groundwater depth, on the contrary, exhibited a smooth increase during this period due to the groundwater regulation by HGSD since 1975 (Fig. 7a and b) (Kasmarek et al., 2012; Yu et al., 2014). It should be noted that most of the ground water pumping wells in the HG area are drilled to depths of up to 300–600 m below the surface while the hydrocarbon wells are drilled to an average depth of 1066 m in Texas ("Energy & Capital"). In addition, the subsidence center at Seabrook nearly followed the distribution of wells from both land and sea (Fig. 8b and c). Therefore, we are confident that the observed subsidence over the Seabrook oil field was not caused by groundwater withdrawals but hydrocarbon extraction. Furthermore, our InSAR time-series measurements indicate a subsidence rate of about 30 mm/yr during the 1990s (Fig. 8b) which reduced to a subsidence rate of less than 10 mm/yr during 2003–2009 (Fig. 8c). Our land surface deformation observations agree with the production activity of the wells at Seabrook oil field: most wells were built around 1985–1990, some of them stopped working around 2005–2010, and no active wells at the present (Drilling Info's database's, 2014). Thus, the hydrocarbon extraction should be wholly responsible for the observed local subsidence over Seabrook oil filed.

Fig. 8. Enlarged deformation maps at hydrocarbon exploration fields whose locations are outlined by pink dashed rectangles and labeled as A–F in Fig. 4: (a) Webster (A in Fig. 4) from ERS; (b, c) Seabrook (B in Fig. 4) from ERS and Envisat, respectively; (d, e) Goose Creek field (C in Fig. 4) from ERS and Envisat, respectively; (f–h) Barbers Hill (D in Fig. 4) from ERS, Envisat, and ALOS, respectively; (i–k) Stratton Ridge (E in Fig. 4) from ERS, Envisat, and ALOS, respectively; (l, m) Santa Fe (F in Fig. 4) from ERS and Envisat, respectively; (n) North Dayton (G in Fig. 4) from ALOS. Dark open cycles represent active wells working at present. Purple open cycles show the other working wells that operated intermittently. Black crosses are the injection wells. For simplicity, inactive wells and dry hole are not shown. Detailed description of wells can be found in Drilling Info's database's (2014). Light purple ellipsoids in (i–k) display the positions of Stratton Ridge dome, and the North Dayton salt dome is also outlined in (n). (For interpretation of the references to color in this figure legend, the reader is referred to the web version of this article.)

Our InSAR results indicate a ~35 mm/yr subsidence cone over the Stratton Ridge oil field (Fig. 8i–k). The spatial extent of the subsidence cone matches the distribution of active wells located at the eastern part of Stratton Ridge dome (light purple ellipsoid in Fig. 8i–k). The InSAR map from the ALOS dataset (Fig. 8k) has much higher coherence than those from ERS-1/2 (Fig. 8i) and Envisat (Fig. 8j) because the longer wavelength of L-band RADAR is less likely to penetrate the tree canopy at random depths as is the case with shorter wavelength C-Band radar. Despite the relatively low coherence of C-band data at nonurban area, ERS and Envisat data still record similar results as that from ALOS (Fig. 8i and k). As the specific type of the listed active wells is unavailable, the observed subsidence is likely due to hydrocarbon/brine exploration or related to salt dome movement, which will be further discussed at a later section.

The Santa Fe oil field (F in Fig. 4) is located in Galveston County, Texas. A 10 mm/yr subsidence feature is detected by both ERS and Envisat data over the oil production field (Fig. 8l, m). Subsidence can also be observed at North Dayton oil field, which experienced an elevation loss of about 15 mm/yr from 2009 to 2011 (Fig. 8n). Besides the petroleum wells, the North Dayton salt dome is also displayed (Fig. 8n), where a local uplift in the center of salt dome is surrounded by subsidence. The observed pattern of these fluctuations in surface elevation may be a result of both salt dome movement and oil production.

In summary, our InSAR results have measured subsidence at 8 oil fields, where hydrocarbon exploration played the dominant role in the observed subsidence. In other cases, observed deformation is likely related to salt dome movement.

5.3. Salt Dome movement and its influence on faults and land subsidence

Some salt domes in the Houston region are experiencing active diapirism, causing the uplift in the surface above the salt dome field (Engelkemeir, Khan, & Burke, 2010). A salt dome is a type of structural dome created when a thick bed of evaporate minerals (mainly halite) found at depth intrudes vertically into surrounding rock strata, forming a diapir (Schultz-Ela, Jackson, & Vendeville, 1993). Naturally, active diapirism can cause uplift in the surface above the salt dome field (Schultz-Ela et al., 1993). On the other hand, salt domes are important in petroleum geology since the salt structures are impermeable and can cause the formation of a stratigraphic trap. Emptied salt domes can be used to store natural gas, so they have been used extensively by industry for brining operations and for the storage of liquid hydrocarbons, refined products, and natural gas as mentioned earlier. Salt domes are widely distributed in the U.S., all are located near or in the Gulf of Mexico, where were an ancient sea until the Jurassic age (Jackson & Vendeville, 1994). However, the number, size, and shape of mapped salt domes vary from one investigation to another. Two publications (Huffman et al., 2004; O'Neill & Van Siclen, 1984) that reported ~30 salt domes over our study area are adopted for our discussion (Fig. 9a): the pink dash circles show the salt dome locations drawn by Huffman et al. (2004) while the black dash circles indicate the spatial extents of salt domes by O'Neill and Van Siclen (1984). One possibility for the subsidence over the HG area could be the continued withdrawal of the subsurface salt. However, if salt domes in the region are still experiencing active diapirism, localized uplift can be observed such as the case over the North Dayton (Fig. 8n). The combined diapirism and mining of salt domes can result in uplift in the surface above the salt domes and subsidence of the surrounding area, or vice versa (Engelkemeir et al., 2010; Khan et al., 2014). We next present two observations to illustrate the possibility of salt movement in HG area: Stratton Ridge and Humble salt domes.

The Stratton Ridge salt dome is a large salt diapir located about 15 km from the currently active Strategic Petroleum Reserve Site at Bryan Mound, Texas (Lord, Rautman, & Looff, 2006). It is roughly oval in outline, with its long axis oriented southwest to northeast (Fig. 10a) (Huffman et al., 2004). Numerous shallow and cavern-related wells have been drilled on the flanks since about 1922, and constructed between the 1950s and the 1970s. The caprock geometry of the Stratton Ridge salt dome is remarkable (Fig. 10). The top of the eastern one-third of the Stratton Ridge dome is depressed at least 1000 ft. with respect to the western two thirds (Fig. 10b). Furthermore, within that structurally low eastern one-third area is a north–south elongated "basin" (Lord et al., 2006). The subsidence (negative deformation) cone at Stratton Ridge oil field (Figs. 8k and 10a), discovered by ALOS data, appears to present the same trend, i.e. down to the east and up to the west. This pattern of deformation agrees with the 3D model map of the Stratton Ridge salt dome, showing the geometry of the top of the caprock in Lord et al., 2006 (Fig. 10b). Vertical growth of the salt pillows creates pressure on the upward surface, causing extension and faulting. Surface subsidence can thus occur above a shallow salt diapir due to the differential movement of the underlying salt. The observed subsidence cone therefore is likely mainly related to ongoing differential movement of individual salt spines or to lateral movement at the caprock–salt interface.

InSAR-derived deformation map (Fig. 9a) shows a change in the surface elevation of the Humble salt domes. The observed subsidence at the Humble salt dome was approximately 10 mm/yr less than the surrounding during 1993–2000 (ERS, Fig. 9b and c). Holzer and Bluntzer (1984) also showed a positive differential deformation rate at Humble salt dome, i.e. deformation that was larger than twice of the deformation in the surrounding area. Jackson and Seni (1983) showed that the Texas salt domes have a rate of uplift of approximately 0.45 mm/yr. Pittman (1994) noted the maximum uplift of the salt domes in HG area followed closely to Jackson and Talbot's (1986) rates. The uplift at Humble salt dome field is associated with shallow salt domes that partly occupy the aquifer system.

5.4. Faults activity and its correlation with land subsidence

The extraction of hydrocarbon and water causes a decline in pore pressure within the hydrocarbon reservoir and alters the stress state near the fault (Morton, 2003). Subsurface fluid extraction has activated surface faults throughout the HG during the past several decades. Many of these faults are extensions of subsurface Tertiary faults and run parallel to the coastline (Buckley et al., 2003; Gabrysch & Coplin, 1990; Verbeek & Clanton, 1981). The geologic activities in salt dome are undoubtedly one of the most important factors in inducing faulting as most (~80%) of the faults in the HG area occur over salt domes (Engelkemeir & Khan, 2008). Fault-related subsidence has been recorded in several locations around HG. The subsidence rates vary with locations, but some areas have a subsidence rate of several centimeters per year in northwestern HG (Buckley et al., 2003; Engelkemeir & Khan, 2008).

Changes in subsidence gradient are observed over most of the faults (Fig. 11), demonstrating a strong correlation between the faults and the observed subsidence in the HG region. Two sides of a fault normally have different surface displacements (Fig. 11). The presence of faults can disrupt the integrity of ground water flow, and restrict the horizontal migration of subsidence features, aggravate localized subsidence, (Fig. 11). On one hand, large localized subsidence gradients weaken the surface tension of soil and promote the relative motion between two blocks of a fault. On the other hand, the formation of fault discontinues the integrity of ground water flow, restricts the horizontal spread of subsidence cones, and accelerates localized subsidence. Our InSAR results have demonstrated that ground subsidence due to excessive ground water withdrawals has exacerbated the faults in HG. For example, significant amount of land subsidence over the NWH accelerated the development of faults, causing the faults to evolve with time (Engelkemeir & Khan, 2008; O'Neill & Van Siclen, 1984; Shaw & Lanning-Rush, 2005).

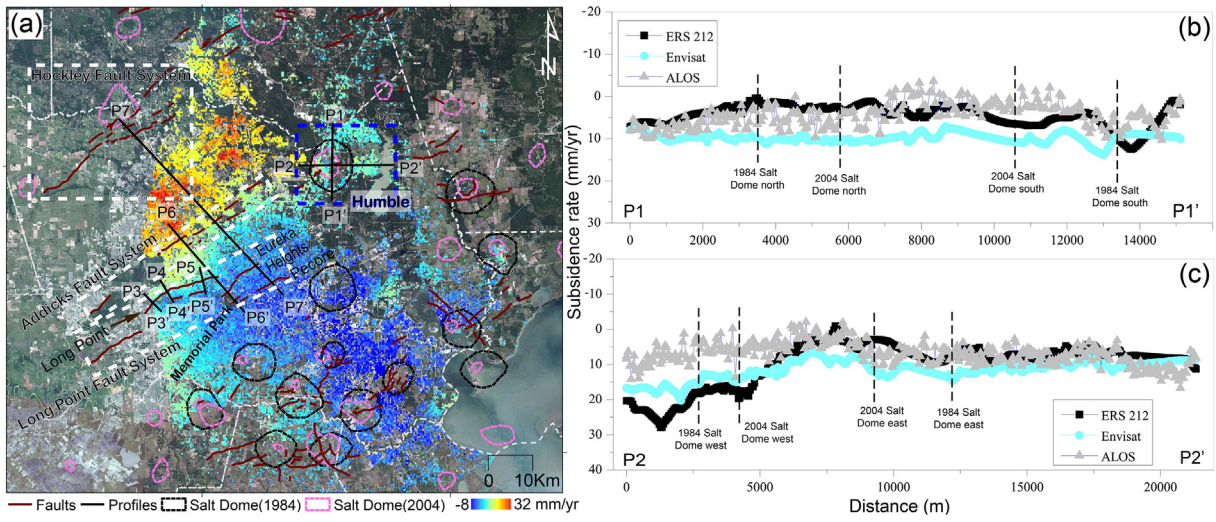

Fig. 9. (a) Map of average deformation rate of Houston Metropolitan area within Harris County, Texas. Black dash circles show salt domes mapped by O'Neill et al. in 1984 while the pink dash circles display salt domes mapped by Huffman et al. in 2004. Faults are labeled in dark red lines, and three main active fault systems are framed with white dash rectangles. Black lines represent profiles across the Humble salt dome and active faults; (b, c) InSAR-derived deformation along the two profiles across the Humble salt dome. Dash lines indicate edges of the Humble Salt dome in 1984 and 2004. (For interpretation of the references to color in this figure legend, the reader is referred to the web version of this article.)

Finally, the fault activities correlate with the spatial distributions of ground subsidence. The fault movement in HG area is caused by water-level decline and the associated subsidence in the region (Coplin & Galloway, 1999). Based on our InSAR result, the faults in the western part of HG were intensively active during 1993–2000, with a creep rate of 15–25 mm/yr at Long Point fault system, about 40 mm/yr at Addicks fault system and 15 mm/yr at Hockley fault system (Fig. 11). The fault activity corresponded well to significant land subsidence occurring over the western HG during 1993–2000. Fault activities during 2005–2012 dramatically decreased to 5–20 mm/yr at all the three fault systems due to the migration of the subsidence cone toward the northern HG and the rising of ground water level. Fault activities stopped or slowed in the area of stable or uplift deformation area, i.e. water-level recovery, but continued unabatedly in the area of ongoing subsidence area and water-level decline.

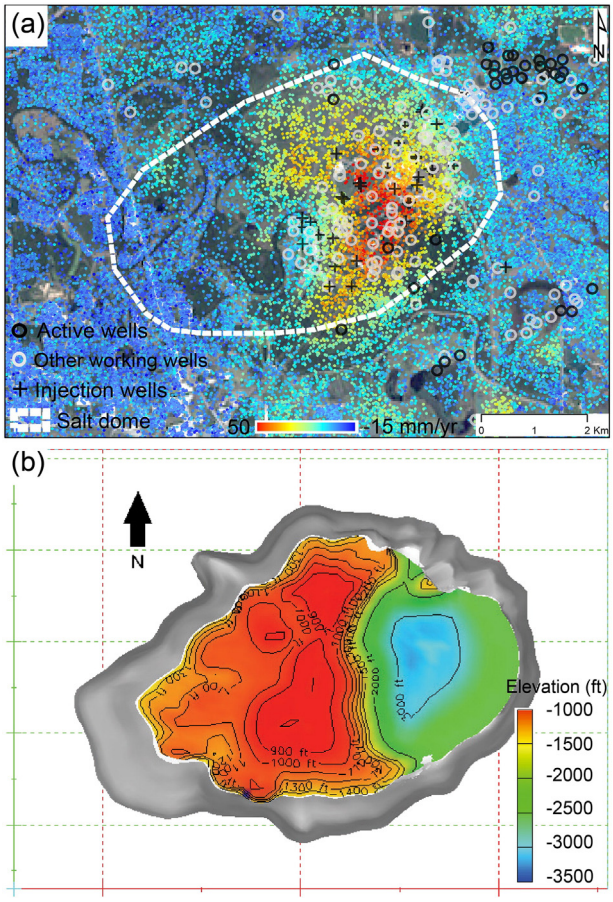

Fig. 10. (a) The subsidence map from MTI analysis of ALOS data. The locations of wells over the salt dome are superimposed on the subsidence map. (b) 3D map of the Stratton Ridge salt dome, showing the geometry of the top of the caprock (Lord et al., 2006).

6. Conclusions

We used the MTI technique combined with GPS and extensometer data to assess nearly two decades of spatially and temporally varied land surface deformation in the HG region associated with the groundwater withdrawal, hydrocarbon exploration and production, halite diapirism, and fault activity. First, based on our MTI results, the deformation of HG region can generally be characterized as subsidence in the northwest and uplift in the southeast from 1993 to 2011. The subsidence rates in the northwestern region have decreased from a high of ~53 mm/yr during 1990s to a maximum of ~30 mm/yr during 2004–2011 while the uplift remains at 20 mm/yr in the southeastern region. The peak land subsidence is found in the Jersey Village in the northwestern HG, where subsidence rates reached 53 mm/yr during 1990s. High rates of subsidence in the HG region appear to be decreasing, and the lateral extent of subsidence is shrinking and migrating toward the northeast. Second, using GPS and extensometer observations, we report that the accuracy of our InSAR measurements of long-term subsidence can reach 11 mm/yr. Third, our study has found strong spatial and temporal correlation between fluid withdrawal and the subsequent subsidence measured using InSAR: the greater the ground water-level drop. Fourth, our InSAR results have identified localized subsidence in 8 active hydrocarbon exploration fields throughout the region. Depressurization of a producing field can lead to reservoir compaction, movement of the overburden and subsidence of the ground surface above the active production wells. As a result, local subsidence features could be formed around the active hydrocarbon exploration wells. Therefore, both groundwater and hydrocarbon withdrawal in parts of HG are considered to be the major drivers of the observed surface deformation. Fifth, the MTI technique has allowed us to identify subtle deformation patterns over salt domes. The ongoing differential

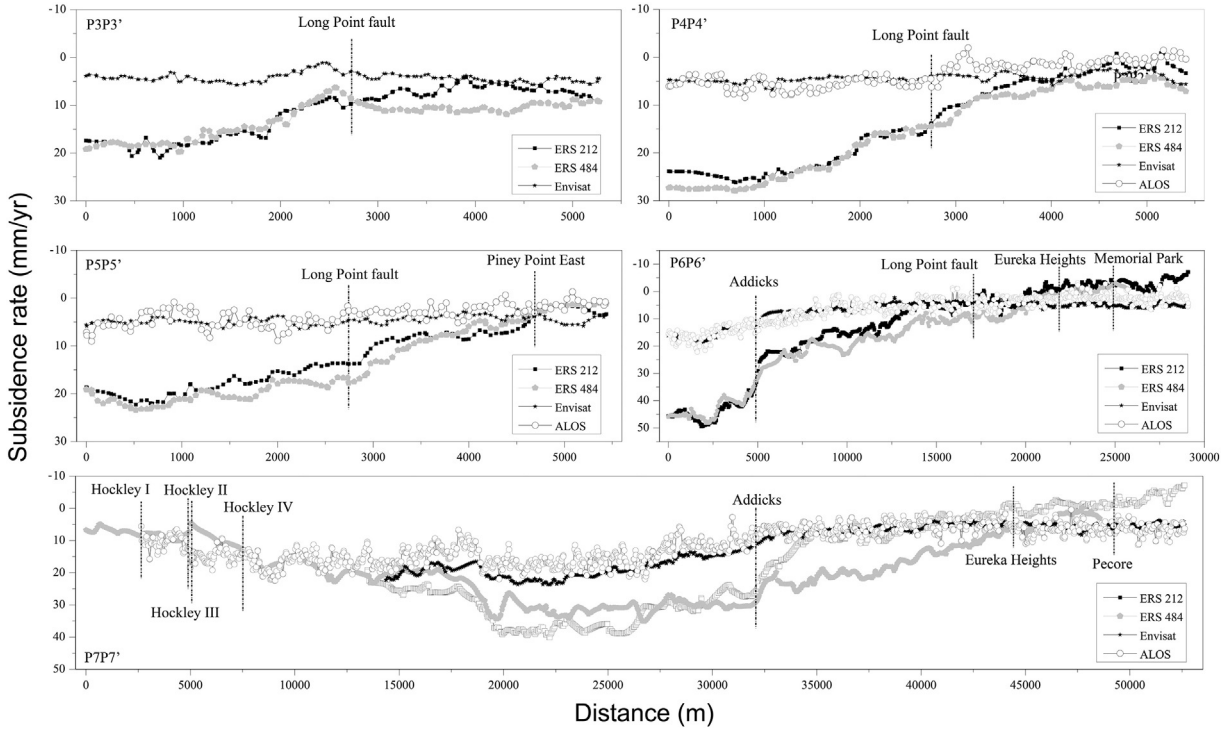

Fig. 11. Land subsidence from four InSAR datasets along the five profiles whose positions are marked on Fig. 10a. Dash lines indicate locations of faults.

movement associated with individual salt spines or at the caprock–salt interface may generate localized subsidence features. Finally, there is an approximately 5–40 mm/yr of differential subsidence across several previously recognized faults. The presence of faults can discontinue the integrity of ground water flow, introduce localized surface displacements, and limit the horizontal spread of subsidence funnels. Therefore, surface subsidence in Houston could be related to a variety of causes including fluid withdrawal (water and hydrocarbon), salt dome activity, and surface faulting.

The MTI technique used in this study has enabled us to conduct the most comprehensive InSAR analysis for the HG region to date, and allowed us to characterize the spatial and temporal deformation patterns that were not possible with traditional InSAR in previous studies. Particularly, advanced MTI InSAR techniques that effectively exploit persistent scatterers and distributed scatterers with adaptive filtering to increase the spatial density of useful measurements (e.g., Ferretti et al., 2011; Parizzi & Brcic, 2011) will provide precise and economically viable methods to measure land subsidence, and therefore play an important role in mitigating the associated geo-hazards. The recent introduction of new radar satellites (Sentinel-1, TerraSAR-X, and ALOS PALSAR-2) will enable us to continuously monitor the subsiding areas in HG region at a finer spatial and temporal resolution to minimize the undesired geo-hazards caused by groundwater withdrawal and hydrocarbon production.

Supplementary data to this article can be found online at http://dx.doi.org/10.1016/j.rse.2015.08.027.

Acknowledgements

This research was supported by the Doctor Postgraduate Technical Project of Chang'an University (Grant No. 2013G5260004), the projects of the National Natural Science Foundation of China (NSFC) (project Nos: 41274004, 41274005, 41304016, 41372375 and 41202189), and National Program on Key Basic Research Project(973 Program) (Grant No. 2014CB744703). Feifei Qu would also like to thank China Scholarship Council for funding her study at Southern Methodist University. Zhong Lu was supported by the Shuler-Foscue Endowment at Southern Methodist University. 1 arc-seconds SRTM DEMs are freely downloaded from http://dds.cr.usgs.gov/srtm/version2_1/. Thanks go to the StaMPS software package, which can be freely downloaded from http://homepages.see.leeds.ac.uk/~earahoo/stamps/index.html. All Ground water data used in the study are archived in the USGS National Water Information System (NWIS), which are freely downloaded from http://waterdata.usgs.gov/nwis/gw. Salt dome data are freely downloaded from http://certmapper.cr.usgs.gov/data/gulf/gulflib/spatial/shape/gcdiapirg.zip. Drilling Info's database of oil/gas wells are acquired from Drillinginfo, Inc. at http://info.drillinginfo.com/.

References

Amelung, F., Galloway, D. L., Bell, J., Zebker, H. A., & Laczniak, R. (1999). Sensing the ups and downs of Las Vegas: InSAR reveals structural control of land subsidence and aquifer-system deformation. *Geology*, *27*(6), 483–486.

Ashworth, J. B., & Hopkins, J. (1995). Aquifers of Texas. *Texas Water Development Board Report 345*. Austin, TX: Texas Water Development Board.

Baker, E. T. (1979). Stratigraphic and hydrogeologic framework of part of the coastal plain of Texas. *Texas Department of Water Resources Report 236*. Austin, TX: Texas Department of Water Resources (18 pp.).

Baker, E. T. (1986). Hydrology of the JasperAquifer in the southeast Texas coastal plain. *Texas Department of Water Resources Report 295*. Austin, TX: Texas Department of Water Resources (33 pp.).

Bawden, G. W., Johnson, M. R., Kasmarek, M. C., Brandt, J., & Middleton, C. S. (2012). Investigation of land subsidence in the Houston–Galveston region of Texas by using the global positioning system and interferometric synthetic aperture radar, 1993–2000. *U.S. Geological Survey Scientific Investigations report 2012–5211* (88 pp.).

Bawden, G. W., Thatcher, W., Stein, R. S., Hudnut, K. W., & Peltzer, G. (2001). Tectonic contraction across Los Angeles after removal of groundwater pumping effects. *Nature*, *412*, 812–815.

Berardino, P., Fornaro, G., Lanari, R., & Sansosti, E. (2002). A new algorithm for surface deformation monitoring based on small baseline differential interferograms. *IEEE Transactions on Geoscience and Remote Sensing*, *40*(11), 2375–2383.

Buckley, S. M., Rosen, P. A., Hensley, S., & Tapley, B. D. (2003). Land subsidence in Houston, Texas, measured by radar interferometry and constrained by extensometers. *Geophysical Research*, *108*(B11) (18 pp.).

Burbey, T. (2002). The influence of faults in basin-fill deposits on land subsidence, Las Vegas valley, Nevada, USA. *Hydrogeology Journal*, *10*(5), 525–538.

Carr, J. E., Meyer, W. R., Sandeen, W. M., & McLane, I. R. (1985). Digital models for simulation of ground-water hydrology of the Chicot and Evangeline aquifers along the Gulf Coast of Texas. *Texas Department of Water Resources report 289* (101 pp.).

Chowdhury, A. H., & Turco, M. J. (2006). Geology of the Gulf Coast Aquifer, Texas. *Texas Water Development Board report 365* (pp. 23–50) (at http://www.twdb.texas.gov/publications/reports/numbered_reports/doc/R365/R365_Composite.pdf).

Cigna, F., Osmanoğlu, B., Cabral-Cano, E., Dixon, T. H., Ávila-Olivera, J. A., Garduño-Monroy, V. H., ... Wdowinski, S. (2012). Monitoring land subsidence and its induced geological hazard with Synthetic Aperture Radar Interferometry: a case study in Morelia, Mexico. *Remote Sensing of Environment*, *117*, 146–161.

Coplin, L. S., & Galloway, D. (1999). Houston–Galveston, Texas—Managing coastal subsidence. In D. Galloway, D. R. Jones, & S. E. Ingebritsen (Eds.), *Land subsidence in the United States: U.S. Geological Survey Circular*, *1182*. (pp. 35–48).

Ding, X. L., Liu, G. X., Li, Z. W., Li, Z. L., & Chen, Y. Q. (2004). Ground subsidence monitoring in Hong Kong with satellite SAR interferometry. *Photogrammetric Engineering & Remote Sensing*, *70*(10), 1151–1156.

Drilling Info's database (2014). Retrieved from http://info.drillinginfo.com

Energy & Capital. Retrieved from http://www.energyandcapital.com/resources/the-depth-of-oil-wells.

Engelkemeir, R., & Khan, S. D. (2008). Lidar mapping of faults in Houston, Texas, USA. *Geosphere*, *4*(1), 170–182.

Engelkemeir, R., Khan, S. D., & Burke, K. (2010). Surface deformation in Houston, Texas using GPS. *Tectonophysics*, *490*, 47–54.

Ferretti, A., Fumagalli, A., Novali, F., Prati, C., Rocca, F., & Rucci, A. (2009). Exploitation of distributed scatterers in interferometric data stacks. *International Geoscience Remote Sensing Symposium (IGARSS), Cape Town, South Africa*.

Ferretti, A., Fumagalli, A., Novali, F., Prati, C., Rocca, F., & Rucci, A. (2011). A new algorithm for processing interferometric data-stacks: SqueeSAR. *IEEE Transactions on Geoscience and Remote Sensing*, *49*(9), 3460–3470.

Ferretti, A., Prati, C., & Rocca, F. (2001). Permanent scatterers in SAR interferometry. *IEEE Transactions on Geoscience and Remote Sensing*, *39*, 8–20.

Fort Bend Subsidence District (2013). Fort Bend Subsidence District 2013 Regulatory Plan. 16 pp., at http://www.fbsubsidence.org/docs_reports/2015/20130828_FBSD_Regulatory_Plan_ADOPTED_(FINAL).pdf

Fruneau, B., & Sarti, F. (2000). Detection of ground subsidence in the city of Paris using radar interferometry: Isolation of deformation from atmospheric artifacts using correlation. *Geophysical Research Letters*, *27*(24), 3981–3984.

Gabrysch, R. K., & Coplin, L. S. (1990). Land-surface subsidence resulting from ground-water withdrawals in the Houston–Galveston region, Texas, through 1987*90-01*, 1–53.

Gabrysch, R. K. (1984). Ground-water withdrawals and land-surface subsidence in the Houston–Galveston region, Texas, 1906–80. *Texas Water Development Board Report 287*. Austin, TX: Texas Department of Water Resources (at https://www.twdb.texas.gov/publications/reports/numbered_reports/doc/R287/R287.pdf).

Gabrysch, R. K., & Bonnet, C. W. (1975). Land surface subsidence in the Houston–Galveston region, Texas. *Texas Water Development Board report 188*. Austin, TX: Texas Department of Water Resources (at https://www.twdb.texas.gov/publications/reports/numbered_reports/doc/R188.pdf).

Harris-Galveston Subsidence District (2013a). Regulatory plan 2013. (14 pp., at) http://hgsubsidence.org/wp-content/uploads/2013/07/HGSD-2013-Regulatory-Plan-with-Amendment.pdf; (http://hgsubsidence.org/subsidence-data/).

Harris-Galveston Subsidence District (2013b). 2013 annual groundwater report. (182 pp., Friendswood, TX, at http://hgsubsidence.org/documents/).

Heleno, S. I. N., Oliveira, L. G. S., Henriques, M. J., Falcão, A. P., Lima, J. N. P., Cooksley, G., ... Fonsaca, J. F. B. D. (2011). Persistent scatterers interferometry detects and measures ground subsidence in Lisbon. *Remote Sensing of Environment*, *115*(8), 2152–2167.

HGSD (2005). Harris-Galveston subsidence district. http://www.subsidence.org/Measure/Extensometers.html

HGSD (2014). Harris-Galveston subsidence district. http://hgsubsidence.org

Holzer, T. L., & Bluntzer, R. L. (1984). Land subsidence near oil and gas-fields, Houston, Texas. *Ground Water*, *22*(4), 450–459.

Hooper, A. (2007). A combined multi-temporal InSAR method incorporating persistent scatterer and small baseline approaches. *ESA Fringe 2007 Workshop, Frascati, Italy*.

Hooper, A. (2008). A multi-temporal InSAR method incorporating both persistent scatterer and small baseline approaches. *Geophysical Research Letters*, *35*, L16302.

Hooper, A., & Zebker, H. (2007). Phase unwrapping in three dimensions with application to InSAR time series. *Journal of the Optical Society of America A. Optics and Image Science*, *24*, 2737–2747.

Hooper, A., Zebker, H., Segall, B., & Kampes, B. (2004). A new method for measuring deformation on volcanoes and other natural terrains using InSAR persistent scatterers. *Geophysical Research Letters*, *31*, L23611.

Hooper, H., Segall, P., & Zebker, H. (2007). Persistent scatterer interferometric synthetic aperture radar for crustal deformation analysis, with application to Volcán Alcedo, Galápagos. *Journal of Geophysical Research: Solid Earth (1978–2012)*, *112*, B07407. http://dx.doi.org/10.1029/2006JB004763.

Huffman, A. C., Kinney, S. A., Biewick, L. R. H., Mitchell, H. R., & Gunther, G. L. (2004). *Gulf coast geology (GCG) online — Miocene of southern Louisiana: U.S. Geological Survey Data SeriesDS-90-A, version 1.0.* Denver, Colorado: U.S. Geological Survey, Central Energy Resources Team.

Jackson, M. P. A., & Seni, S. J. (1983). Geometry and evolution of salt structures in a marginal rift basin of the Gulf of Mexico, east Texas. *Geology*, *11*, 131–135.

Jackson, M. P. A., & Talbot, C. J. (1986). External shapes, strain rates, and dynamics of salt structures. *Geological Society of America Bulletin*, *97*, 305–323.

Jackson, M. P. A., & Vendeville, B. C. (1994). Regional extension as a geologic trigger for diapirism. *Geological Society of America Bulletin*, *106*, 57–73.

Joaquim, J. S., Hooper, A., Hanssen, R., Bastos, L., & Ruiz, A. (2011). Persistent scatterer InSAR: A comparison of methodologies based on a model of temporal deformation vs. spatial correlation selection criteria. *Remote Sensing of Environment*, *115*, 2652–2663.

Johnson, M. R., Ramage, J. K., & Kasmarek, M. C. (2011). Water-level altitudes 2011 and water-level changes in the Chicot, Evangeline, and Jasper aquifers and compaction 1973–2010 in the Chicot and Evangeline aquifers, Houston–Galveston region. *Texas: U.S. Geological Survey Scientific Investigations Map*, *3174*, (17 pp., 16 sheets).

Jorgensen, D. G. (1975). *Analog-model studies of ground-water hydrology in the Houston District, Texas*. Houston, Texas: U. S. Geological Society.

Kampes, K., Hanssen, R., & Perski, Z. (2003). Radar interferometry with public domain tools. *Proceedings of FRINGE 2003, ESA/ESRIN, Frascati, Italy*.

Kasmarek, M. C., & Robinson, J. L. (2004). Hydrogeology and simulation of groundwater flow and land-surface subsidence in the northern part of the Gulf Coast aquifer system, Texas. *U.S. Geological Survey Scientific Investigations Report 2004–5102* (111 pp.).

Kasmarek, M. C., & Strom, E. W. (2002). Hydrogeology and simulation of ground-water flow and land-surface subsidence in the Chicot and Evangeline aquifers, Houston Area. *Texas: U.S. Geological Survey Water-Resources Investigation Report 02–4022* (61 pp.).

Kasmarek, M. C., Johnson, M. R., & Ramage, J. K. (2010). Water-level altitudes 2010 and water-level changes in the Chicot, Evangeline, and Jasper aquifers and compaction 1973–2009 in the Chicot and Evangeline aquifers, Houston–Galveston region. *Texas: U.S. Geological Survey Scientific Investigations Map 3138* (17 pp., 16 sheets).

Kasmarek, M. C., Johnson, M. R., & Ramage, J. K. (2012). Water-level altitudes 2012 and water-level changes in the Chicot, Evangeline, and Jasper aquifers and compaction 1973–2011 in the Chicot and Evangeline aquifers, Houston–Galveston region, Texas. In C.E.R.T.U.S. Geological Survey (Ed.), *U.S. Geological Survey Scientific Investigations Map 3230*.

Khan, S. D., Stewart, R. R., Otoum, M., & Chang, L. (2013). A geophysical investigation of the active Hockley Fault System near Houston, Texas. *Geophysics*, *78*(4), B177–B185.

Khan, S. D. (2014). *Surface Deformation in the Northern Gulf of Mexicohttp://www.uh.edu/~sdkhan/research_gom.html*

Khan, S. D., Huang, Z., & Karacay, A. (2014). Study of ground subsidence in northwest Harris County using GPS, LiDAR, and InSAR techniques. *Natural Hazards*.

Lanari, R., Mora, O., Manunta, M., Mallorqui, J. J., Berardino, P., & Sansosti, E. (2004). A small-baseline approach for investigating deformations on full-resolution differential SAR interferograms. *IEEE Transactions on Geoscience and Remote Sensing*, *42*, 1377–1386.

Lord, A. S., Rautman, C. A., & Looff, K. M. (2006). In S.N. Laboratories (Ed.), *Geologic technical assessment of the Stratton ridge salt dome, Texas, for potential expansion of the U.S. Strategic petroleum reserve* (pp. 42). *U.S.* Department of Commerce.

Lu, Z., & Danskin, W. (2001). InSAR analysis of natural recharge to define structure of a ground-water basin, San Bernardino, California. *Geophysical Research Letters*, *28*, 2661–2664.

Lu, Z., & Dzurisin, D. (2014). *InSAR imaging of Aleutian volcanoes: Monitoring a volcanic arc from space*. Springer Praxis Books, Geophysical Sciences978-3-642-00347-9 (390 pp.).

Lu, Z., & Zhang, L. (2014). Frontiers of radar remote sensing. *Photogrammetric Engineering & Remote Sensing*, *80*(1), 5-1.

Lu, Z., Dzurisin, D., Jung, H. S., Zhang, J. X., & Zhang, Y. H. (2010). Radar image and data fusion for natural hazards characterization. *International Journal of Image and Data Fusion*, *1*, 217–242.

Massonnet, D., Rossi, M., Carmona, C., Adragna, F., Peltzer, G., Feigl, K., & Rabaute, T. (1993). The displacement field of the landers earthquake mapped by radar interferometry. *Nature*, *364*(6433), 138–142.

Mora, O., Mallorqui, J. J., & Broqustas, A. (2003). Linear and nonlinear terrain deformation maps from a reduced set of interferometric SAR images. *IEEE Transactions on Geoscience and Remote Sensing*, *41*(10), 2243–2253.

Morton, R. A. (2003). An Overview of Coastal Land Loss: With Emphasis on the Southeastern United States. *U.S. Geological Survey Open File Report 03–337* (24 pp.).

O'Neill, V. C., & Van Siclen, D. C. (1984). Activation of Gulf Coast faults by depressuring of aquifers and an engineering approach by siting structures along their traces. *Bulletin of the Association of Engineering Geologists*, *XXI*(1), 73–87.

Parizzi, A., & Brcic, R. (2011). Adaptive InSAR stack multilooking exploiting amplitude statistics: A comparison between different techniques and practical results. *IEEE Geoscience and Remote Sensing Letters*, *8*(3), 441–445.

Peltzer, G., & Rosen, P. (1995). Surface displacement of the 17 May 1993 Eureka Valley, California, *Earthquake observed by SAR interferometry*. *Science*, *268*(5215), 1333–1336.

Perissin, D., & Wang, T. (2010). Time-series InSAR applications over urban areas in China. *IEEE Journal of Selected Topics in Applied Earth Observations and Remote Sensing*, *4*(1), 92–100.

Pittman, D. W. (1994). *Growth history and structural analysis of Sugarland dome, fort bend county, Texas.* (Master Thesis) Houston, Texas: University of Houston.

Pratt, W. E., & Johnson, D. W. (1926). Local subsidence of the Goose Creek oil field. *Journal of Geology*, *34*, 577–590.

Qu, F., Zhang, Q., Lu, Z., Zhao, C. Y., Yang, C. S., & Zhang, J. (2014). Land subsidence and ground fissures in Xi'an, China 2005–2012 revealed by multi-band InSAR time-series analysis. *Remote Sensing of Environment*, *155*, 366–376.

Schmidt, D. A., & Bürgmann, R. (2003). Time dependent land uplift and subsidence in the Santa Clara Valley, California, from a large InSAR data set. *Journal of Geophysical Research*, *108*(B9).

Schultz-Ela, D. D., Jackson, M. P. A., & Vendeville, B. C. (1993). Mechanics of active salt diapirism. *Tectonophysics*, *228*, 215–312.

Seifert, J., & Drabek, C. (2006). History of production and potential future production of the Gulf Coast Aquifer. (chap. 16 of) In R. E. Mace, S. C. Davidson, E. S. Angle, & W. F. MullicanIII (Eds.), *Aquifers of the gulf coast of Texas: Texas Water Development Board Report 365* (pp. 261–271).

Shaw, S. D., & Lanning-Rush, J. (2005). *Principal faults in the Houston, Texas, metropolitan area.* U. S. Geological Survey Scientific Investigations Map 2874.

Smith, J. C. (2010). *"HUMBLE OILFIELD," handbook of Texas online.* (http://www.tshaonline.org/handbook/online/articles/doh07, published by the) Texas State Historical Association.

Stork, S. V., & Sneed, M. (2002). *Houston–Galveston bay area, Texas, from space—A new tool for mapping land subsidence.* U.S. Geological Survey Fact Sheet 110-02 (6 pp.).

Tesauro, M., Berardino, P., Lanari, R., Sansosti, E., Fornaro, G., & Franceschetti, G. (2000). Urban subsidence inside the city of Napoli (Italy) observed by satellite radar interferometry. *Geophysical Research Letters*, *27*(13), 1961–1964.

Verbeek, E. R., & Clanton, U. S. (1981). Historically active faults in the Houston metropolitan area, Texas. In E. M. Etter (Ed.), *Houston area environmental geology: Surface faulting, ground subsidence, hazard liability*. Houston, TX: Houston Geol. Soc.

Verbeek, E. R., Ratzlaff, K. W., & Clanton, U. S. (1979). Faults in parts of north-central and western Houston metropolitan area. *Texas: U.S. Geological Survey Miscellaneous Field Studies Map MF-1136, 1 sheet*.

Wang, G., Yu, J., Kearns, T. J., & Ortega, J. (2014). Assessing the accuracy of long-term subsidence derived from borehole extensometer data using GPS observations: Case study in Houston, Texas. *Journal of Surveying Engineering*, *05014001*http://dx.doi.org/10.1061/(ASCE)SU.1943-5428.0000133.

Werner, C., Wegmuller, U., Strozzi, T., & Wiesmann, A. (2003). Interferometric point target analysis for deformation mapping. *International Geoscience and Remote Sensing Symposium*. Toulouse, France: Geosci. & Remote Sens. Soc.

Yu, J. B., Wang, G. Q., Kearns, T. J., & Yang, L. Q. (2014). Is there deep-seated subsidence in the Houston–Galveston area. *International Journal of Geophysics*, *2014* (11 pp.).

Zebker, H. A., & Villaseno, J. (1992). Decorrelation in interferometric radar echoes. *IEEE Transactions on Geoscience and Remote Sensing*, *30*(5), 950–959.

Zebker, H. A., Rosen, P. A., Goldstein, R. M., Gabriel, A., & Werner, C. L. (1994). On the derivation of coseismic displacement fields using differential radar interferometry: The Landers earthquake. *Journal of Geography Research*, *99*, 19617–19634.

Zhang, L., Lu, Z., Ding, X. L., Jung, H. S., Feng, G. C., & Lee, C. W. (2012). Mapping ground surface deformation using temporarily coherent point SAR interferometry: Application to Los Angeles Basin. *Remote Sensing of Environment*, *117*, 429–439.